

# High-resolution X-ray luminescence extension imaging

<https://doi.org/10.1038/s41586-021-03251-6>

Received: 1 August 2020

Accepted: 11 December 2020

Published online: 17 February 2021

 Check for updates

Xiangyu Ou<sup>1,8</sup>, Xian Qin<sup>2,8</sup>, Bolong Huang<sup>3,8</sup>, Jie Zan<sup>1</sup>, Qinxia Wu<sup>1</sup>, Zhongzhu Hong<sup>1</sup>, Lili Xie<sup>1</sup>, Hongyu Bian<sup>2</sup>, Zhigao Yi<sup>2</sup>, Xiaofeng Chen<sup>1</sup>, Yiming Wu<sup>2</sup>, Xiaorong Song<sup>1</sup>, Juan Li<sup>1</sup>, Qiushui Chen<sup>1,5</sup>✉, Huanghao Yang<sup>1,5</sup>✉ & Xiaogang Liu<sup>2,4,6,7</sup>✉

Current X-ray imaging technologies involving flat-panel detectors have difficulty in imaging three-dimensional objects because fabrication of large-area, flexible, silicon-based photodetectors on highly curved surfaces remains a challenge<sup>1–3</sup>. Here we demonstrate ultralong-lived X-ray trapping for flat-panel-free, high-resolution, three-dimensional imaging using a series of solution-processable, lanthanide-doped nanoscintillators. Corroborated by quantum mechanical simulations of defect formation and electronic structures, our experimental characterizations reveal that slow hopping of trapped electrons due to radiation-triggered anionic migration in host lattices can induce more than 30 days of persistent radioluminescence. We further demonstrate X-ray luminescence extension imaging with resolution greater than 20 line pairs per millimetre and optical memory longer than 15 days. These findings provide insight into mechanisms underlying X-ray energy conversion through enduring electron trapping and offer a paradigm to motivate future research in wearable X-ray detectors for patient-centred radiography and mammography, imaging-guided therapeutics, high-energy physics and deep learning in radiology.

Flat-panel X-ray detectors with active readout mechanisms have found critical applications in medical diagnostics, security screening and industrial inspection<sup>4</sup>. Over recent decades, several types of X-ray detector—mainly based on direct conversion of X-ray energy into electrical charges or indirect conversion using a scintillating material—have been implemented<sup>5–8</sup>. Many X-ray detection technologies require integration of flat-panel detectors with thin-film transistors (TFTs) consisting of pixelated photodiode arrays deposited on glass substrates. Although TFT-integrated flat-panel detectors offer high sensitivity for X-ray detection and radiographic reconstruction, they present substantial challenges for high-resolution X-ray imaging. Moreover, flat-panel detectors are costly and not applicable to three-dimensional (3D) X-ray imaging of curved or irregularly shaped objects. Despite enormous efforts, flexible X-ray detectors have not been well developed due to stringent dual requirements of a flexible TFT substrate and a thin layer of scintillators conformably attached to the flexible substrate.

Persistent luminescent phosphors can store excitation energy and slowly release the captured energy as light emission<sup>9–12</sup>, making it possible to develop flat-panel-free X-ray detectors. Although inorganic oxide phosphors, such as SrAl<sub>2</sub>O<sub>4</sub>:Eu<sup>2+</sup>/Dy<sup>3+</sup> and ZnGa<sub>2</sub>O<sub>4</sub>:Cr<sup>3+</sup> (ZGO:Cr), have been used for in vivo optical imaging under X-ray irradiation<sup>13</sup>, these materials suffer from low X-ray sensitivity<sup>14</sup>. Moreover, their fabrication also requires complex crystal growth processes under harsh conditions (>600 °C) to generate efficient electron-trapping

states in host lattices<sup>15</sup>. Persistent luminescent microparticles can be prepared by mechanical grinding<sup>12</sup>. However, microparticles are difficult to disperse in solution for thin-film processing, a prerequisite for the fabrication of flexible devices.

Lanthanide-doped nanomaterials that exhibit unique luminescence properties<sup>16,17</sup> have been widely used in X-ray scintillation<sup>3,18–20</sup>, optical imaging<sup>21,22</sup>, biosensing<sup>23</sup> and optoelectronics<sup>24</sup>. Notably, high-energy irradiation at ambient conditions can displace small anions from their lattice to interstitial sites, creating vacancy and interstitial pairs<sup>25</sup>. Here we report a general approach for flat-panel-free X-ray imaging of 3D electronic objects using lanthanide-doped nanoscintillators that feature high-efficiency X-ray absorption and long-lived energy trapping. We name this imaging technique X-ray luminescence extension imaging (Xr-LEI) for its ability to perform radiography on highly curved 3D objects after the termination of X-rays, which is inaccessible by conventional flat-panel X-ray detectors or synchrotron-based X-ray microscopy.

We synthesized a series of terbium (Tb<sup>3+</sup>)-doped NaLuF<sub>4</sub> nanoscintillators by a co-precipitation method<sup>22</sup> (Extended Data Figs. 1, 2). A representative transmission electron microscopy (TEM) micrograph of oleic acid-capped NaLuF<sub>4</sub>:Tb(15 mol%)/NaYF<sub>4</sub> core-shell nanoscintillators reveals a hexagonal shape with an average size of 27 nm (Fig. 1a). The radioluminescence of NaLuF<sub>4</sub>:Tb@NaYF<sub>4</sub> nanoscintillators was measured under excitation with a 50-kV X-ray source (Fig. 1b). We observed a set of intense emission bands, corresponding to <sup>5</sup>D<sub>4</sub> → <sup>7</sup>F<sub>4</sub> (584 nm),

<sup>1</sup>MOE Key Laboratory for Analytical Science of Food Safety and Biology and State Key Laboratory of Photocatalysis on Energy and Environment, College of Chemistry, Fuzhou University, Fuzhou, China. <sup>2</sup>Department of Chemistry, National University of Singapore, Singapore, Singapore. <sup>3</sup>Department of Applied Biology and Chemical Technology, The Hong Kong Polytechnic University, Hong Kong SAR, China. <sup>4</sup>Joint School of National University of Singapore and Tianjin University, Tianjin University, Fuzhou, China. <sup>5</sup>Fujian Science and Technology Innovation Laboratory for Optoelectronic Information of China, Fuzhou, China. <sup>6</sup>Center for Functional Materials, National University of Singapore Suzhou Research Institute, Suzhou, China. <sup>7</sup>The N.I. Institute for Health, National University of Singapore, Singapore, Singapore. <sup>8</sup>These authors contributed equally: Xiangyu Ou, Xian Qin, Bolong Huang. ✉e-mail: qchen@fzu.edu.cn; hhyang@fzu.edu.cn; chmlx@nus.edu.sg

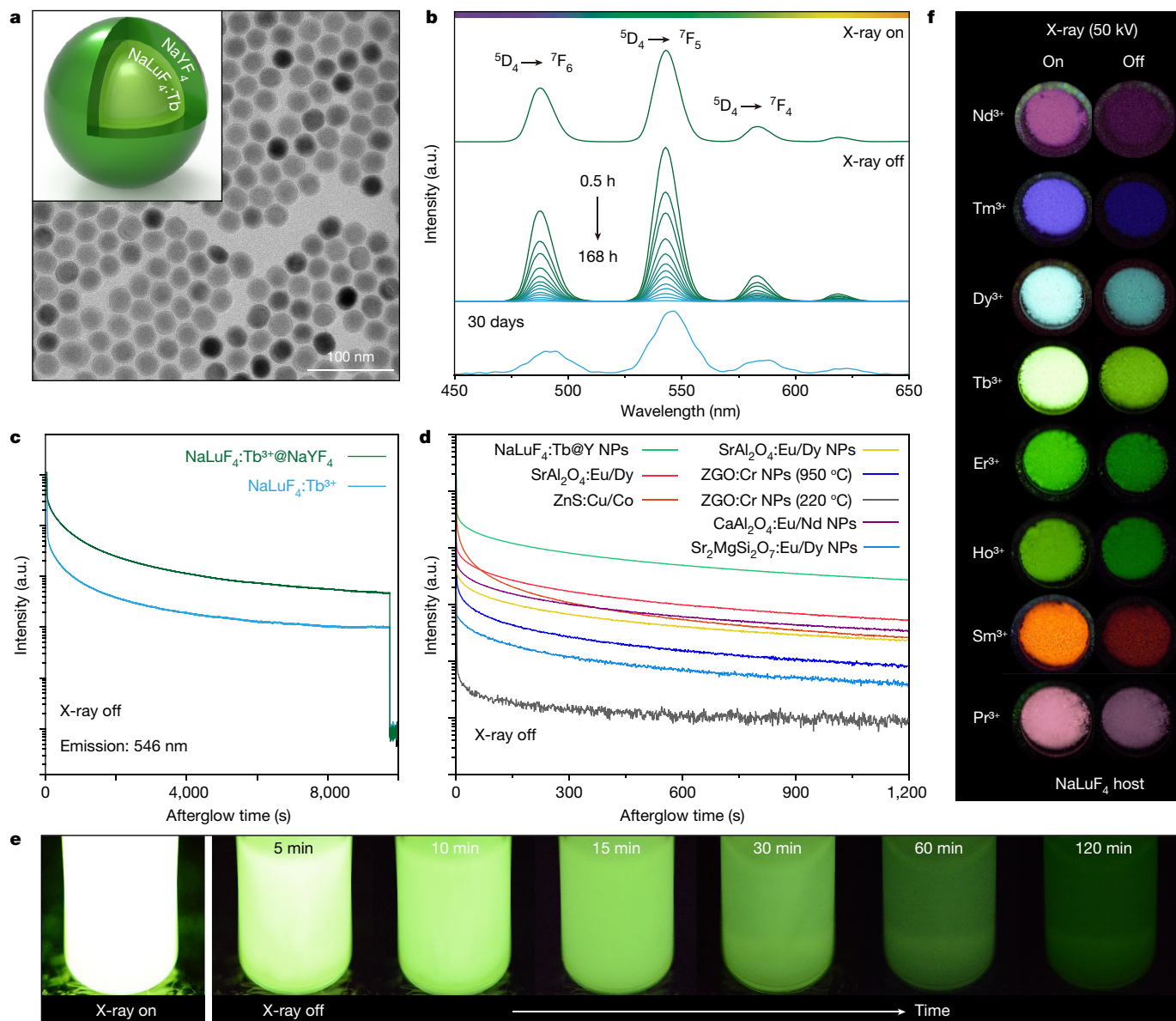


**Fig. 1 | Characterization of lanthanide-doped persistent luminescent nanoscrolls.** **a**, TEM micrograph of NaLuF<sub>4</sub>:Tb(15 mol%)/NaYF<sub>4</sub> nanocrystals. **b**, Radioluminescent emission spectra of the core-shell nanocrystals, recorded after cessation of X-rays (50 kV) for 0.5–168 h or 30 days. **c**, Radioluminescent intensity of NaLuF<sub>4</sub>:Tb(15 mol%) and NaLuF<sub>4</sub>:Tb(15 mol%)/NaYF<sub>4</sub> nanocrystals, monitored at 546 nm as a function of time upon cessation of X-rays. **d**, Comparison of afterglow decay profiles of

various phosphors after cessation of X-ray excitation (50 kV). NPs, nanoparticles. **e**, Afterglow photographs of NaLuF<sub>4</sub>:Tb(15 mol%)/NaYF<sub>4</sub> nanocrystals dispersed in 1 ml cyclohexane. X-ray operation was set at a voltage of 70 kV with a tube current of 1 mA. **f**, Radioluminescence and afterglow of NaLuF<sub>4</sub> nanocrystals doped with various activators (Nd<sup>3+</sup>, Tm<sup>3+</sup>, Dy<sup>3+</sup>, Tb<sup>3+</sup>, Er<sup>3+</sup>, Ho<sup>3+</sup>, Sm<sup>3+</sup> and Pr<sup>3+</sup>). a.u., arbitrary units.

$^5D_4 \rightarrow ^7F_5$  (546 nm) and  $^5D_4 \rightarrow ^7F_6$  (489 nm) optical transitions of Tb<sup>3+</sup>. On switching off the X-ray source, we recorded prolonged radioluminescence decay of these nanoscrolls with gradually decreasing intensity (Fig. 1b, c, Extended Data Fig. 3, Supplementary Video 1), suggesting effective trapping of ionizing radiation. Intriguingly, the afterglow emission of NaLuF<sub>4</sub>:Tb@NaYF<sub>4</sub> nanoscrolls lasted more than 30 days after the termination of X-rays (Fig. 1b, bottom). By comparison, the afterglow lifetime of previously reported ZnGa<sub>2</sub>O<sub>4</sub>:Cr<sup>3+</sup> phosphors is approximately 15 days<sup>12</sup>. We also observed a gradual increase in the emission intensity of NaLuF<sub>4</sub>:Tb@NaYF<sub>4</sub> nanoscrolls on continuous X-ray irradiation, indicating a dynamic energy-charging process (Extended Data Fig. 3). Importantly, our nanomaterials cannot be activated by daylight, making them ideal for fabrication of X-ray memory devices. Notably, coating of a NaYF<sub>4</sub> shell onto NaLuF<sub>4</sub>:Tb nanoparticles

enhanced the radioluminescence intensity by 1.5-fold, whereas the afterglow luminescence intensity was increased by 6.5-fold (Fig. 1c). These results suggest that NaYF<sub>4</sub>-shell passivation can effectively mitigate quenching of trapped X-ray energies on nanocrystal surfaces.

We next benchmarked the radioluminescence of NaLuF<sub>4</sub>:Tb(15 mol%)/NaYF<sub>4</sub> nanoscrolls with commercial plastic scintillators and conventional persistent phosphors, including SrAl<sub>2</sub>O<sub>4</sub>:Eu<sup>2+</sup>/Dy<sup>3+</sup> powder, ZnS:Cu<sup>2+</sup>/Co<sup>2+</sup> powder, SrAl<sub>2</sub>O<sub>4</sub>:Eu<sup>2+</sup>/Dy<sup>3+</sup> nanoparticles and ZnGa<sub>2</sub>O<sub>4</sub>:Cr<sup>3+</sup> nanoparticles. Under X-ray irradiation at 50 kV, our core-shell nanoscrolls exhibited much stronger X-ray-induced emission and afterglow luminescence than commercial counterparts (Fig. 1d, Extended Data Fig. 4, Supplementary Fig. 1, Supplementary Table 1). Improvements in performance were attributed to the large X-ray stopping power and high X-ray trapping efficiency of NaLuF<sub>4</sub>:



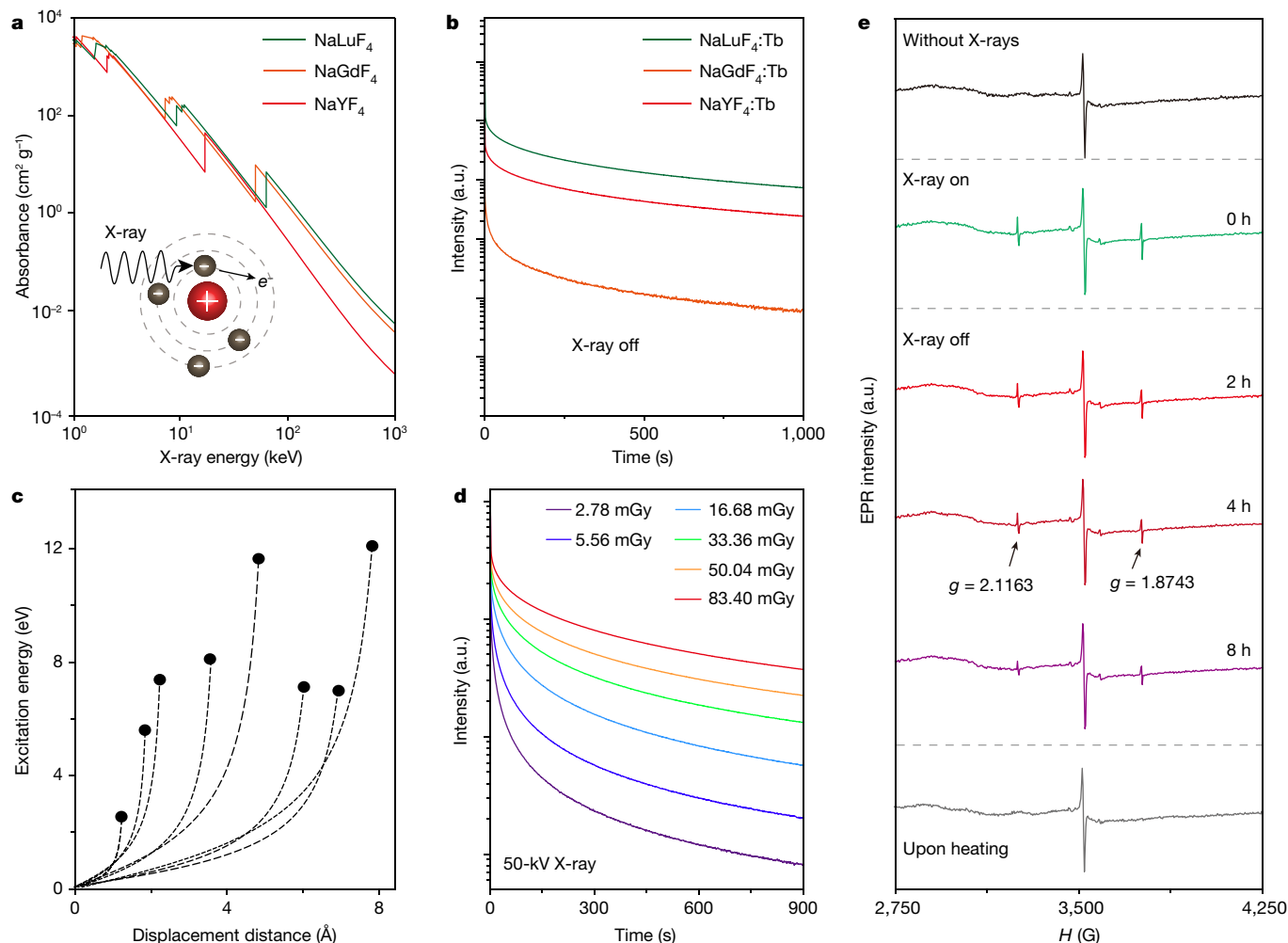


**Fig. 2 | Photophysical studies of X-ray irradiation on lanthanide-doped nanoscrintillators.** **a**, Absorption spectra of NaYF<sub>4</sub>, NaGdF<sub>4</sub> and NaLuF<sub>4</sub> as a function of X-ray energy. Attenuation coefficients were obtained from ref.<sup>26</sup>. The inset shows a schematic of X-ray-induced photoionization. **b**, Room-temperature afterglow intensity of NaYF<sub>4</sub>:Tb (15 mol%), NaGdF<sub>4</sub>:Tb (15 mol%) and NaLuF<sub>4</sub>:Tb (15 mol%) nanocrystals as a function of time after cessation of X-rays. All samples were excited with X-rays at 50 kV.

**c**, Dependence of transient formation energy on the separation distance between the V<sub>F</sub> and I<sub>F</sub> subdefects. **d**, Decay curves of the NaLuF<sub>4</sub>:Tb (15 mol%) nanocrystals when illuminated with different X-ray dosages at room temperature. **e**, EPR spectra of as-synthesized NaLuF<sub>4</sub>:Tb (15 mol%) nanocrystals. Samples were measured at room temperature under the following conditions: before X-rays, during X-rays, 2, 4 and 8 h after cessation of X-rays, and after heating at 200 °C, respectively. *H*, magnetic field.

Tb@NaYF<sub>4</sub> nanoscrintillators. These oleic acid-capped nanoscrintillators emit radioluminescence visible to the unaided eye upon switching off the X-ray source (70 kV, 1 mA) (Fig. 1e). Moreover, multicolour radioluminescence modulation from the ultraviolet–visible to the near-infrared can be achieved using hexagonal-phase NaLuF<sub>4</sub> nanocrystals as a host material for activator doping (for example, Nd<sup>3+</sup>, Tm<sup>3+</sup>, Dy<sup>3+</sup>, Tb<sup>3+</sup>, Er<sup>3+</sup>, Ho<sup>3+</sup>, Sm<sup>3+</sup> and Pr<sup>3+</sup>) (Fig. 1f, Extended Data Fig. 5). Notably, there is no detectable afterglow of Eu<sup>3+</sup>-doped nanoparticles after X-ray charging (Extended Data Fig. 6).

To understand how large-momentum X-ray photons interact with lanthanide-doped nanoscrintillators to produce lasting radioluminescence, we examined the X-ray photon-absorbing ability of the NaLuF<sub>4</sub> host<sup>26,27</sup>. The absorption coefficient of NaLuF<sub>4</sub> (atomic number *Z*<sub>max</sub> = 71, *K*α = 63.31 keV) is larger than that of NaYF<sub>4</sub> (*Z*<sub>max</sub> = 39, *K*α = 17.05 keV) or NaGdF<sub>4</sub> (*Z*<sub>max</sub> = 64, *K*α = 50.24 keV) (Fig. 2a). Indeed, the afterglow intensity of NaLuF<sub>4</sub>:Tb (15 mol%) nanocrystals is threefold stronger than that of NaYF<sub>4</sub>:Tb (15 mol%) nanocrystals, suggesting a heavy-atom (for example, Lu<sup>3+</sup>) effect on X-ray absorption (Fig. 2b). The high-efficiency radioluminescence was also attributed to the low phonon energy of the hexagonal-phase NaLuF<sub>4</sub> crystal lattice (<350 cm<sup>-1</sup>) and reduced surface quenching. Moreover, at a low Gd<sup>3+</sup> concentration, the excitation

energy can be efficiently transferred from Gd<sup>3+</sup> to Tb<sup>3+</sup> activators. By comparison, at a high Gd<sup>3+</sup> concentration, the excitation energy dissipates non-radiatively to quenching sites through energy migration, resulting in fast spontaneous emission of Tb<sup>3+</sup> with low afterglow intensity (Extended Data Fig. 6).

We further investigated long-lived X-ray energy trapping by modelling the formation of anion Frenkel defects in a NaLuF<sub>4</sub> lattice. We speculated that a sufficient energy may dislocate fluoride anions (F<sup>-</sup>) to interstitial sites through elastic collisions with large-momentum X-ray photons<sup>25,28</sup> (Extended Data Fig. 7). This leads to formation of fluoride vacancies (V<sub>F</sub>) and interstitials (I<sub>F</sub>), accompanied by the production and trapping of many energetic electrons (e<sup>-</sup>) in Frenkel defect-associated trap states. Using first-principles calculations based on density functional theory (DFT), we monitored the structural relaxation of anion Frenkel pairs at various distances. We found that interstitial fluoride ions gradually diffuse back to original vacancies when the proximity of these two subdefects is less than 3 Å. For defect pairs with a larger separation (more than 3 Å), interstitial fluoride ions can be stabilized due to increased energy barriers, except under stimulation with heating or light exposure. Creation of such defect pairs requires formation energies from 2.78 eV to 12 eV, suggesting a high probability of

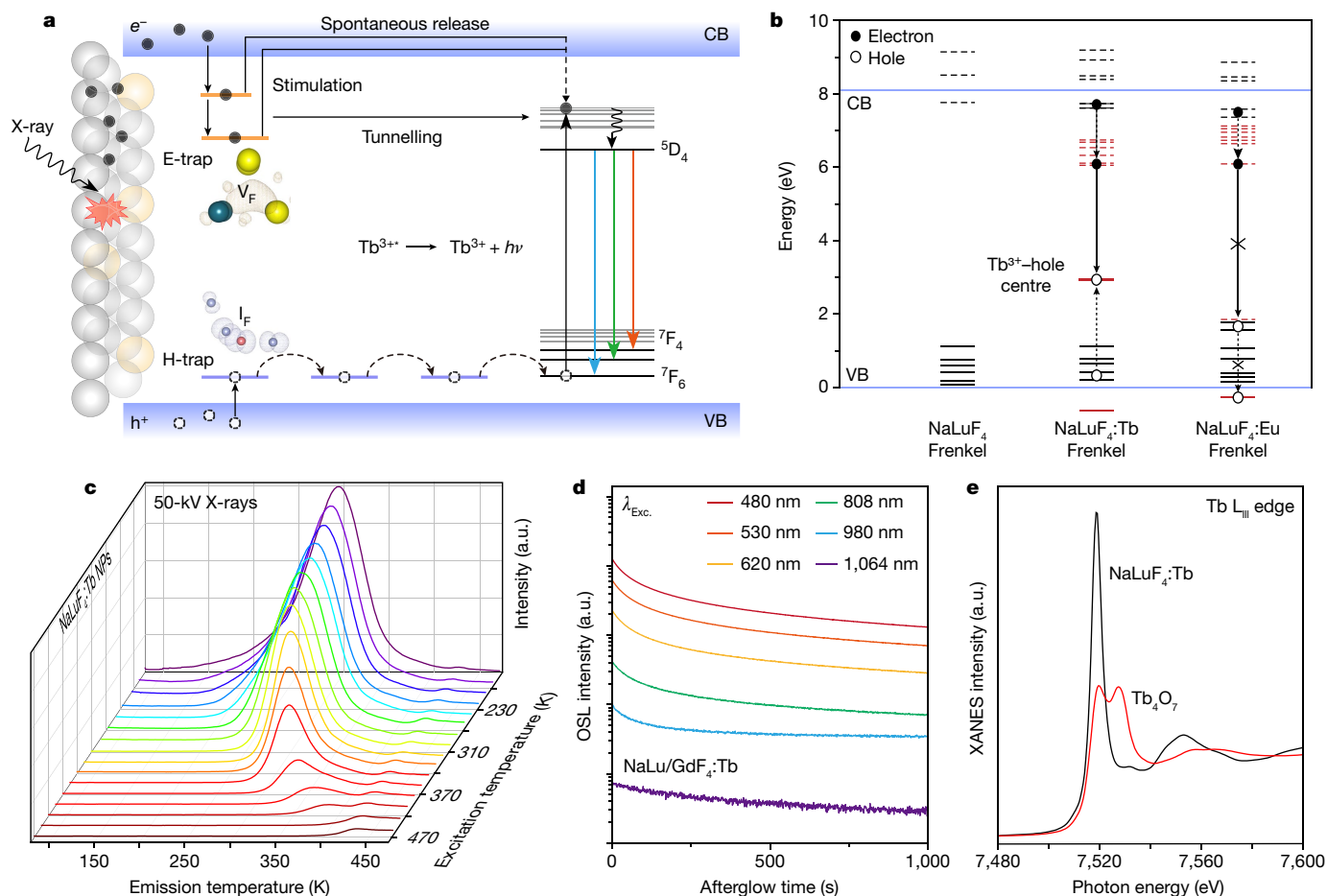


**Fig. 3 | Mechanistic investigations of X-ray energy trapping in lanthanide-doped nanoscintillators.** **a**, Proposed mechanism of long-lived persistent radioluminescence of Tb<sup>3+</sup>-doped NaLuF<sub>4</sub> nanocrystals. Upon X-ray excitation, electrons at an inner electronic shell of lattice atoms are photoexcited to produce low-energy electrons, which are either transferred to activators for emission or partially stored at electronic trap states. Electrons in shallow traps release slowly for spontaneous long-lasting emission of Tb<sup>3+</sup>. In contrast, electrons in deep traps populate to the conduction band (CB) under optical or thermal stimulation. VB, valence band. **b**, Energy diagram of lanthanide 4f levels (in red) with respect to host bands (in black). Solid and dotted lines represent occupied and empty orbitals, respectively. **c**, Thermally

stimulated luminescence spectra of NaLuF<sub>4</sub>:Tb (15 mol%) nanocrystals measured in the temperature range of 170 to 470 K. The sample was first irradiated by an X-ray source for 300 s. After cessation of the X-ray source for 10 min, emission spectra were measured at a heating rate of 1 K s<sup>-1</sup>. **d**, Optically stimulated luminescence (OSL) decay profiles of NaLuF<sub>4</sub>:Tb/Gd (15/5 mol%) nanocrystals, recorded upon turning off X-rays and photostimulation at 480, 530, 620, 808, 980 and 1,064 nm for 2 min, respectively. All measurements were performed at room temperature 1 h after luminescence afterglow of the samples faded.  $\lambda_{\text{Exc}}$ , excitation wavelength. **e**, X-ray absorption near-edge structure (XANES) spectra of the Tb L<sub>III</sub> edge, recorded from NaLuF<sub>4</sub>:Tb (15 mol%) nanocrystals and Tb<sub>4</sub>O<sub>7</sub> reference samples.

displacing fluoride ions upon X-ray irradiation (Fig. 2c). Moreover, DFT calculations revealed that for defect pairs with small separation distances, electron relaxation and atom diffusion have similar rates (Extended Data Fig. 7). With an increase in separation distance, the rate of electron relaxation decreases, owing to substitution-based anion diffusion, rather than direct relaxation.

We next examined the transient dynamics of X-ray energy trapping at Frenkel defects by varying the X-ray dosage. Our experiments indicated that afterglow intensity can be enhanced with higher doses, most likely owing to an increased density of trap states available for X-ray storage (Fig. 2d). We further measured captured electrons at trap states by electronic paramagnetic resonance (EPR) spectroscopy. After cessation of X-ray excitation, we observed a gradual decrease in EPR signal intensity ( $g = 1.8743$  and  $g = 2.1163$ ; where  $g$  is a scaling factor accounting for the coupling between orbital and spin angular momentum), and the EPR signal completely disappeared upon heating at 200 °C for 20 min (Fig. 2e). These results confirm that it is possible to generate high-density trap states in lanthanide-doped nanoscintillators using high-momentum X-ray photons and subsequently to achieve long-lived photon trapping.

In light of experimental and computational results, we proposed the following mechanism underlying long-lived photon trapping in lanthanide-doped nanoscintillators (Fig. 3a). In a NaLuF<sub>4</sub>:Tb (15 mol%) nanoscintillator, X-ray energies are primarily absorbed by lutetium atoms in the lattice to create many energetic electrons, largely due to photoelectric effects. Through elastic collisions of large-momentum X-ray photons with small fluoride ions, anion Frenkel defects form in the nanocrystal and trap thermalized low-energy electrons, enabling long-lived photon trapping. Specifically, fluoride vacancies and interstitials are created as electron traps (E-traps) and hole traps (H-traps). Displacements of fluoride ions at short and long distances form transient shallow and long-lived deep trap states, respectively. Electrons in shallow traps can spontaneously escape over time to the conduction band with a concurrent defect self-healing process, whereas electrons in deep traps require extra energy in the form of either optical or thermal stimulation to migrate to Tb<sup>3+</sup> emitters. Trapped holes can also migrate towards Tb<sup>3+</sup> emitters, forming hole–Tb<sup>3+</sup> centres that radiatively recombine with captured electrons. Notably, we did not observe Eu<sup>3+</sup> emission as hole–Eu<sup>3+</sup> centres could not be formed in

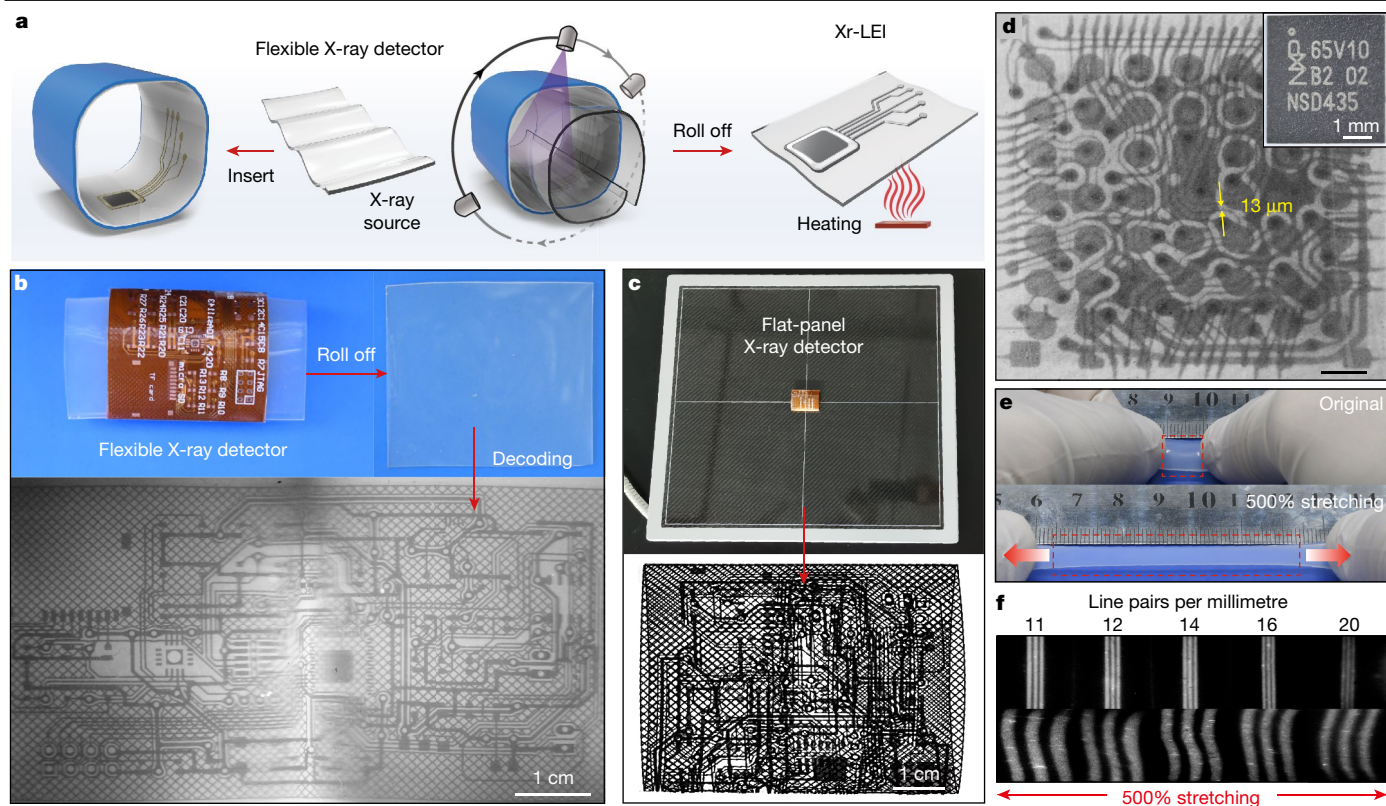


**Fig. 4 | High-resolution Xr-LEI.** **a**, Schematic showing 3D electronic imaging enabled by a nanoscintillator-integrated, flexible detector. First, the detector is inserted into a 3D electronic circuit board for conformal coating. Next, the image of the electronic board is projected onto the detector. After cessation of X-rays, the detector is transferred onto a hot substrate for thermal stimulation and subsequently luminescence imaging. **b**, Xr-LEI of a 3D electronic board using a prototype NaLuF<sub>4</sub>:Tb(15 mol%)/@NaYF<sub>4</sub>-based detector (voltage, 50 kV;

heating temperature, 80 °C). **c**, Imaging of the same circuit board using a conventional flat-panel X-ray detector. **d**, Xr-LEI of integrated circuits of an iPhone 6 Plus smartphone (voltage, 50 kV; scale bar, 500 μm). The inset is the corresponding digital photograph of the circuits. **e**, Photograph of a stretchable, NaLuF<sub>4</sub>:Tb(15 mol%)/@NaYF<sub>4</sub>-based X-ray detector. **f**, High-resolution Xr-LEI using the stretchable X-ray detector (voltage, 50 kV).

Eu<sup>3+</sup>-doped NaLuF<sub>4</sub> compounds on the basis of electronic calculations (Fig. 3b). We measured thermally stimulated luminescence spectra of NaLuF<sub>4</sub>:Tb nanocrystals in the temperature range of 170 to 470 K (Fig. 3c, Supplementary Fig. 2), and the energy distribution of electron trap states was calculated as 0.12–0.98 eV below the conduction band (Extended Data Fig. 8). By optically stimulating stored electrons to escape from deep traps, we confirmed that high-energy photons induce stronger persistent luminescence than low-energy photons (Fig. 3d). The local electronic structure of Tb<sup>3+</sup> was examined by X-ray absorption near-edge spectroscopy, revealing that Tb<sup>3+</sup> activators in NaLuF<sub>4</sub> nanocrystals maintain a trivalent state (Fig. 3e, Supplementary Fig. 3). The core–shell nanoscintillators showed high recyclability and photostability under X-ray irradiation and heating at 80 °C for 14 cycles (Extended Data Fig. 8, Supplementary Video 1).

The ability to trap X-ray energy in nanoscintillators for persistent radioluminescence prompted us to develop a flexible detector for Xr-LEI (Fig. 4a, Extended Data Fig. 9). This detector was fabricated by embedding NaLuF<sub>4</sub>:Tb(15 mol%)/@NaYF<sub>4</sub> nanoscintillators (2 wt%) into a polydimethylsiloxane (PDMS) substrate (16 cm × 16 cm × 0.1 cm). Internal structures of a highly curved electronic circuit board can be visualized using the as-fabricated X-ray detector and a digital camera or smartphone (Fig. 4b). High-resolution 3D Xr-LEI was achieved by combining afterglow luminescence and graphical simulations (Supplementary Video 2). For comparison, only overlapped imaging of the electronic circuit board was rendered using a typical flat-panel X-ray detector (Fig. 4c, Supplementary Fig. 4). Using thin films containing 2.5 wt% NaLuF<sub>4</sub>:Tb(15 mol%)/@NaYF<sub>4</sub> nanoparticles, the X-ray exposure for digital radiography shortened to 1 s (Extended Data Fig. 10).

We further demonstrated high-resolution Xr-LEI using a highly stretchable detector comprising NaLuF<sub>4</sub>:Tb(15 mol%)/@NaYF<sub>4</sub> nanoscintillators and commercial silicone rubber (Fig. 4d, Extended Data Fig. 11, Supplementary Video 3). The stretchable X-ray detector enabled a spatial imaging resolution of more than 20 line pairs per millimetre (<25 μm), which is much higher than that achievable by conventional flat-panel X-ray detectors (typically less than 5.0 line pairs per millimetre) (Fig. 4e, f).

The invention of the Xr-LEI technique enhances our understanding of the microscopic mechanism governing long-lived trapping of X-rays in condensed-matter systems. Our experimental investigations on X-ray-induced generation of Frenkel defect-based trap states offer new opportunities to fabricate persistent luminescent nanocrystals, which are highly desirable for applications in optogenetics, low-dose radiotherapy, optoelectronics, expansion microscopy, and quantification of radioactive particles, such as α, β or high-energy γ particles<sup>29–32</sup>. When coupled with highly stretchable elastomers<sup>33</sup>, these optical nanomaterials may allow the development of next-generation X-ray imaging technologies with unprecedented spatial resolution and special imaging capability for 3D conformal electronics<sup>34</sup>. Such low-cost, smartphone-recordable, X-ray imaging techniques are particularly suitable for point-of-care radiography, screening mammography without breast compression and semiconductor non-destructive inspection.

## Online content

Any methods, additional references, Nature Research reporting summaries, source data, extended data, supplementary information,



acknowledgements, peer review information; details of author contributions and competing interests; and statements of data and code availability are available at <https://doi.org/10.1038/s41586-021-03251-6>.

- Rogers, J. A., Someya, T. & Huang, Y. Materials and mechanics for stretchable electronics. *Science* **327**, 1603–1607 (2010).
- Wang, S. et al. Skin electronics from scalable fabrication of an intrinsically stretchable transistor array. *Nature* **555**, 83–88 (2018).
- Blahuta, S., Bessiere, A., Gourier, D., Ouspenski, V. & Viana, B. Effect of the X-ray dose on the luminescence properties of Ce:LYSO and co-doped Ca,Ce:LYSO single crystals for scintillation applications. *Opt. Mater.* **35**, 1865–1868 (2013).
- Chen, Q. et al. All-inorganic perovskite nanocrystal scintillators. *Nature* **561**, 88–93 (2018).
- Yakunin, S. et al. Detection of X-ray photons by solution-processed organic–inorganic perovskites. *Nat. Photon.* **9**, 444–449 (2015).
- Wei, H. et al. Sensitive X-ray detectors made of methylammonium lead tribromide perovskite single crystals. *Nat. Photon.* **10**, 333–339 (2016).
- Wei, W. et al. Monolithic integration of hybrid perovskite single crystals with heterogenous substrate for highly sensitive X-ray imaging. *Nat. Photon.* **11**, 315–321 (2017).
- Büchele, P. et al. X-ray imaging with scintillator-sensitized hybrid organic photodetectors. *Nat. Photon.* **9**, 843–848 (2015).
- le Masne de Chermont, Q. et al. Nanoprobes with near-infrared persistent luminescence for in vivo imaging. *Proc. Natl Acad. Sci. USA* **104**, 9266–9271 (2007).
- Maldiney, T. et al. The in vivo activation of persistent nanophosphors for optical imaging of vascularization, tumours and grafted cells. *Nat. Mater.* **13**, 418–426 (2014).
- Matsuzawa, T., Aoki, Y., Takeuchi, N. & Murayama, Y. A new long phosphorescent phosphor with high brightness,  $\text{SrAl}_2\text{O}_4:\text{Eu}^{2+}, \text{Dy}^{3+}$ . *J. Electrochem. Soc.* **143**, 2670–2673 (1996).
- Pan, Z. et al. Sunlight-activated long-persistent luminescence in the near-infrared from  $\text{Cr}^{3+}$ -doped zinc gallogermanates. *Nat. Mater.* **11**, 58–63 (2012).
- Xue, Z. et al. X-ray-activated near-infrared persistent luminescent probe for deep-tissue and renewable in vivo bioimaging. *ACS Appl. Mater. Interfaces* **9**, 22132–22142 (2017).
- Song, L. et al. Low-dose X-ray activation of W(VI)-doped persistent luminescence nanoparticles for deep-tissue photodynamic therapy. *Adv. Funct. Mater.* **28**, 1707496 (2018).
- Li, Y. et al. Long persistent phosphors—from fundamentals to applications. *Chem. Soc. Rev.* **45**, 2090–2136 (2016).
- Shyichuk, A. et al. Energy transfer upconversion dynamics in  $\text{YVO}_4:\text{Yb}^{3+}, \text{Er}^{3+}$ . *J. Lumin.* **170**, 560–570 (2016).
- Capobianco, J. A., Vetrone, F., Boyer, J. C., Speghini, A. & Bettinelli, M. Enhancement of red emission ( $^4\text{F}_{9/2} \rightarrow ^4\text{I}_{15/2}$ ) via upconversion in bulk and nanocrystalline cubic  $\text{Y}_2\text{O}_3:\text{Er}^{3+}$ . *J. Phys. Chem. B* **106**, 1181–1187 (2002).
- Van der Heggen, D. et al. Optically stimulated nanodosimeters with high storage capacity. *Nanomaterials* **9**, 1127 (2019).
- Hsu, C.-C., Lin, S.-L. & Chang, C. A. Lanthanide-doped core–shell–shell nanocomposite for dual photodynamic therapy and luminescence imaging by a single X-ray excitation source. *ACS Appl. Mater. Interfaces* **10**, 7859–7870 (2018).
- Nikl, M. & Yoshikawa, A. Recent R&D trends in inorganic single-crystal scintillator materials for radiation detection. *Adv. Opt. Mater.* **3**, 463–481 (2015).
- Liu, Y. et al. Amplified stimulated emission in upconversion nanoparticles for super-resolution nanoscopy. *Nature* **543**, 229–233 (2017).
- Prigozhin, M. B. et al. Bright sub-20-nm cathodoluminescent nanoprobes for electron microscopy. *Nat. Nanotechnol.* **14**, 420–425 (2019).
- Bünzli, J.-C. G. Lanthanide luminescence for biomedical analyses and imaging. *Chem. Rev.* **110**, 2729–2755 (2010).
- Fernandez-Bravo, A. et al. Continuous-wave upconverting nanoparticle microlasers. *Nat. Nanotechnol.* **13**, 572–577 (2018).
- Lushchik, C. B. Creation of Frenkel defect pairs by excitons in alkali halides. *Mod. Probl. Condens. Matter Sci.* **13**, 473–525 (1986).
- Berger, M. J. et al. XCOM: Photon Cross Sections Database (NIST, 2013); <https://www.nist.gov/pml/xcom-photon-cross-sections-database>
- Cooper, D. R., Capobianco, J. A. & Seuntjens, J. Radioluminescence studies of colloidal oleate-capped beta- $\text{Na}(\text{Gd}, \text{Lu})\text{F}_4:\text{Ln}^{3+}$  nanoparticles (Ln = Ce, Eu, Tb). *Nanoscale* **10**, 7821–7832 (2018).
- Kang, M. et al. Resolving the nature of electronic excitations in resonant inelastic X-ray scattering. *Phys. Rev. B* **99**, 045105 (2019).
- Lu, K. et al. Low-dose X-ray radiotherapy–radiodynamic therapy via nanoscale metal–organic frameworks enhances checkpoint blockade immunotherapy. *Nat. Biomed. Eng.* **2**, 600–610 (2018).
- Yang, Y. et al. X-ray-activated long persistent phosphors featuring strong UVC afterglow emissions. *Light Sci. Appl.* **7**, 88 (2018).
- Chen, F., Tillberg, P. W. & Boyden, E. S. Expansion microscopy. *Science* **347**, 543–548 (2015).
- All, A. H. et al. Expanding the toolbox of upconversion nanoparticles for in vivo optogenetics and neuromodulation. *Adv. Mater.* **31**, 1803474 (2019).
- Sun, J. Y. et al. Highly stretchable and tough hydrogels. *Nature* **489**, 133–136 (2012).
- Holler, M. et al. High-resolution non-destructive three-dimensional imaging of integrated circuits. *Nature* **543**, 402–406 (2017).

**Publisher's note** Springer Nature remains neutral with regard to jurisdictional claims in published maps and institutional affiliations.

© The Author(s), under exclusive licence to Springer Nature Limited 2021

## Methods

### Chemicals

Gadolinium (III) acetate hydrate ( $\text{Gd}(\text{CH}_3\text{CO}_2)_3 \cdot x\text{H}_2\text{O}$ , 99.9%), yttrium (III) acetate hydrate ( $\text{Y}(\text{CH}_3\text{CO}_2)_3 \cdot x\text{H}_2\text{O}$ , 99.9%), lutetium (III) acetate hydrate ( $\text{Lu}(\text{CH}_3\text{CO}_2)_3 \cdot x\text{H}_2\text{O}$ , 99.9%), thulium (III) acetate hydrate ( $\text{Tm}(\text{CH}_3\text{CO}_2)_3 \cdot x\text{H}_2\text{O}$ , 99.9%), praseodymium (III) chloride hydrate ( $\text{PrCl}_3 \cdot x\text{H}_2\text{O}$ , 99.9%), neodymium (III) acetate hydrate ( $\text{Nd}(\text{CH}_3\text{CO}_2)_3 \cdot x\text{H}_2\text{O}$ , 99.9%), samarium (III) acetate hydrate ( $\text{Sm}(\text{CH}_3\text{CO}_2)_3 \cdot x\text{H}_2\text{O}$ , 99.9%), terbium (III) acetate hydrate ( $\text{Tb}(\text{CH}_3\text{CO}_2)_3 \cdot x\text{H}_2\text{O}$ , 99.9%), dysprosium (III) acetate hydrate ( $\text{Dy}(\text{CH}_3\text{CO}_2)_3 \cdot x\text{H}_2\text{O}$ , 99.9%), holmium (III) acetate hydrate ( $\text{Ho}(\text{CH}_3\text{CO}_2)_3 \cdot x\text{H}_2\text{O}$ , 99.9%), erbium (III) acetate hydrate ( $\text{Er}(\text{CH}_3\text{CO}_2)_3 \cdot x\text{H}_2\text{O}$ , 99.9%), zinc nitrate hexahydrate ( $\text{Zn}(\text{NO}_3)_2 \cdot 6\text{H}_2\text{O}$ , >99%), gallium (III) nitrate hydrate ( $\text{Ga}(\text{NO}_3)_3 \cdot x\text{H}_2\text{O}$ , 99.9%), chromium (III) nitrate nonahydrate ( $\text{Cr}(\text{NO}_3)_3 \cdot 9\text{H}_2\text{O}$ , 99%), sodium hydroxide ( $\text{NaOH}$ , >98%), ammonium fluoride ( $\text{NH}_4\text{F}$ , >98%), 1-octadecene (ODE, 90%), oleic acid (OA, 90%) and cyclohexane (chromatography grade, 99.7%) were purchased from Sigma-Aldrich. SYLGARD 184 silicone elastomer kit was purchased from Dow Corning. Persistent phosphor powders of  $\text{CaAl}_2\text{O}_4 \cdot \text{Eu}^{2+}/\text{Nd}^{3+}$ ,  $\text{Sr}_2\text{MgSi}_2\text{O}_7 \cdot \text{Eu}^{2+}/\text{Dy}^{3+}$ ,  $\text{SrAl}_2\text{O}_4 \cdot \text{Eu}^{2+}/\text{Dy}^{3+}$  and  $\text{ZnS}:\text{Cu}^{2+}/\text{Co}^{2+}$  were purchased from Xiucal Chemical. Type-38 and Type-74 line-pair charts were purchased from Hua Ruisen Technology Development.  $\text{Tb}_4\text{O}_7$  powder was purchased from Aladdin Biochemical Technology. BC422 plastic scintillator was a mixture of poly(vinyltoluene) and small molecules of 2-(4-*tert*-butylphenyl)-5-(4-biphenyl)-1,3,4-oxadiazole, obtained from Saint-Gobain. ST401 plastic scintillator was purchased from Zhonghelixin. Unless otherwise noted, all chemicals were used without further purification.

### Synthesis of $\beta\text{-NaLuF}_4\text{:Ln/Gd}$ ( $x/(20-x)$ mol%) nanocrystals

OA-capped  $\text{NaLuF}_4\text{:Ln/Gd}$  ( $x/(20-x)$  mol%) ( $\text{Ln}^{3+} = \text{Pr}^{3+}, \text{Nd}^{3+}, \text{Sm}^{3+}, \text{Tb}^{3+}, \text{Dy}^{3+}, \text{Ho}^{3+}, \text{Er}^{3+}$  and  $\text{Tm}^{3+}$ ;  $x = 0.5\text{--}15$ ) nanocrystals were synthesized using a coprecipitation method<sup>22</sup>. In a typical experiment, a mixture of  $\text{Ln}(\text{CH}_3\text{CO}_2)_3 \cdot x\text{H}_2\text{O}$  (0.5 mmol;  $\text{Ln} = \text{Lu}, \text{Gd}, \text{Tb}, \text{Nd}, \text{Sm}, \text{Dy}, \text{Ho}, \text{Er}$  and  $\text{Tm}$ ) or  $\text{PrCl}_3 \cdot x\text{H}_2\text{O}$  in the desired ratio was added into a 50-ml two-neck round-bottom flask containing 5.0 ml OA and 7.5 ml ODE. The mixture was heated to 150 °C under vacuum for 30 min. After cooling to room temperature, 10.0 ml methanol containing 2.0 mmol  $\text{NH}_4\text{F}$  and 1.25 mmol  $\text{NaOH}$  was added to the solution. The resulting solution was vigorously stirred at 50 °C for 30 min, followed by heating at 100 °C under vacuum for another 10 min. The reaction mixture was quickly heated to 300 °C at a rate of 20 °C  $\text{min}^{-1}$  for 1 h under a nitrogen atmosphere with stirring. After cooling to room temperature, the resultant nanocrystals were precipitated by addition of ethanol, collected by 8,000 r.p.m. centrifugation for 5 min, washed with absolute ethanol, dispersed in 4.0 ml cyclohexane and finally stored in a freezer at 4 °C.

### Synthesis of $\beta\text{-NaLuF}_4\text{:Tb/Gd}$ (15/ $x$ mol%) nanocrystals

The synthetic procedure for  $\text{NaLuF}_4\text{:Tb}^{3+}/\text{Gd}^{3+}$  (15/ $x$  mol%;  $x = 0\text{--}35$ ) nanocrystals was identical to the synthesis of  $\text{NaLuF}_4\text{:Tb}^{3+}/\text{Gd}^{3+}$  ( $x/(20-x)$  mol%;  $x = 2\text{--}20$ ) nanocrystals.

### Synthesis of $\beta\text{-NaReF}_4\text{:Tb}$ (15 mol%) nanocrystals

The synthetic procedure for  $\text{NaReF}_4\text{:Tb}$  (15 mol%) ( $\text{Re} = \text{Y}$  or  $\text{Gd}$ ) nanocrystals was identical to the synthesis of  $\text{NaLuF}_4\text{:Tb}$  (15 mol%) nanocrystals except for heating temperature and heating duration. To a 50-ml round-bottom two-necks flask, 5.0 ml OA and 7.5 ml ODE were added with a total amount of 0.5 mmol  $\text{Re}(\text{CH}_3\text{CO}_2)_3 \cdot x\text{H}_2\text{O}$  ( $\text{Re} = \text{Y}, \text{Gd}$  and  $\text{Tb}$ ). The resulting solution was heated at 150 °C for 30 min under stirring and then cooled to room temperature. Afterward, a methanol solution (10.0 ml) containing  $\text{NH}_4\text{F}$  (2.0 mmol) and  $\text{NaOH}$  (1.25 mmol) was added to the solution. This solution was heated at 50 °C for 30 min under stirring. Upon removal of methanol by heating at 100 °C for 10 min, the resulting solution was kept at 295 °C for 1.5 h.

Products were precipitated with ethanol, collected by centrifugation at 8,000 r.p.m. for 10 min, washed with absolute ethanol and finally dispersed in 4.0 ml cyclohexane.

### Synthesis of $\beta\text{-NaLuF}_4\text{:Tb@NaYF}_4$ core-shell nanocrystals

The  $\beta\text{-NaLuF}_4\text{:Tb@NaYF}_4$  core-shell nanocrystals were prepared using an epitaxial growth method. In a typical experiment, 0.5 mmol  $\text{Y}(\text{CH}_3\text{COO})_3 \cdot 4\text{H}_2\text{O}$  in 4.0 ml OA and 16 ml ODE were heated to 150 °C under vacuum for 30 min and then cooled to room temperature. The temperature was then decreased to 50 °C, and 4.0 ml as-prepared core nanocrystals were added to the mixture and heated at 80 °C for 10 min to evaporate cyclohexane. After cooling to room temperature, a solution of 2.0 mmol  $\text{NH}_4\text{F}$  and 1.25 mmol  $\text{NaOH}$  dissolved in 10 ml methanol was added. The resulting mixture was vigorously stirred at 50 °C for 30 min and then heated at 100 °C for 10 min. The reaction mixture was then quickly heated to 295 °C for 1.5 h under a nitrogen atmosphere while stirring. After cooling to room temperature, the resulting core-shell nanocrystals were precipitated by addition of ethanol, collected by centrifugation, washed with absolute ethanol and dispersed in 4 ml cyclohexane.

### Synthesis of $\beta\text{-NaGdF}_4\text{:Tb@NaYF}_4$ core-shell nanocrystals

The synthetic procedure for  $\text{NaGdF}_4\text{:Tb@NaYF}_4$  nanocrystals was identical to the synthesis of  $\text{NaLuF}_4\text{:Tb@NaYF}_4$  nanocrystals.

### Synthesis of $\beta\text{-NaGdF}_4\text{:Eu}$ nanocrystals

The synthetic procedure for  $\text{NaGdF}_4\text{:Eu}$  (15 mol%) nanocrystals was identical to the synthesis of  $\text{NaGdF}_4\text{:Tb}$  (15 mol%) nanocrystals.

### Preparation of $\text{ZnGa}_{1.995}\text{O}_4\text{:Cr}_{0.005}$ persistent luminescent nanoparticles

In a typical procedure, persistent luminescence nanoparticles were prepared by a hydrothermal method, followed by sintering in an inert atmosphere. A solution of  $\text{Zn}(\text{NO}_3)_2 \cdot 6\text{H}_2\text{O}$  (0.2668 g, 0.897 mmol),  $\text{Ga}(\text{NO}_3)_3 \cdot x\text{H}_2\text{O}$  (0.4577 g, 1.7895 mmol) and  $\text{Cr}(\text{NO}_3)_3 \cdot 9\text{H}_2\text{O}$  (0.0018 g, 0.0045 mmol) was added to a round-bottom flask and vigorously stirred at room temperature. The total volume was adjusted to 16 ml by adding ultrapure water. Then, ammonium hydroxide (28 wt%) solution was quickly added to adjust the pH to about 6.5 while a white precipitate gradually formed. After stirring for 30 min, the mixture was transferred to a Teflon-lined autoclave (25 ml). The autoclave was put in an oven at 220 °C. After 12 h reaction, the system was cooled to room temperature. The resulting products were washed with deionized water three times to remove excess inorganic species and subsequently dried at 60 °C overnight. The powder was further sintered in air at 950 °C for 4 h.

### Physical characterization

TEM and high-resolution TEM images were taken on a Tecnai G2 F20 S-TWIN microscope (FEI Nano Ports) operated at an accelerating voltage of 200 kV. Elemental mapping analysis was performed using a scanning transmission electron microscopy and energy-dispersive X-ray spectroscopy equipped with a Tecnai G2 F20 S-TWIN microscope at an accelerating voltage of 120 kV. High-resolution scanning transmission electron microscopy characterization was done with an FEI aberration-corrected Titan Cubed S-Twin transmission electron microscope at an accelerating voltage of 60 kV. Scanning electron microscope characterization was performed on a Verios G4 XHR electron microscope (Thermal Fisher Scientific). Radioluminescent spectra and persistent luminescence decay curves were measured using an Edinburgh FS5 fluorescence spectrophotometer (Edinburgh Instruments) equipped with a miniature X-ray source (Amptek). Thermally stimulated luminescence was measured using an Edinburgh FS5 spectrophotometer coupled with an HFS 600 heating/cooling stage (Linkam Scientific Instruments) and a customized optical fibre. X-ray diffraction patterns were obtained using an X-ray powder diffractometer

(D/MAX-3C, Rigaku) over the angular range of 5–90°. Photographs of X-ray-induced luminescence and radioluminescence-based X-ray imaging were acquired with a digital camera (Nikon, D850 coupled with AF-S Micro-Nikkor 105 mm 2.8G or AF-S Micro-Nikkor 40 mm 2.8G) in an all-manual mode. EPR was carried out using a Bruker model A300 spectrometer recorded at 9.85 GHz. X-ray absorption fine-structure spectra were collected with a BL14W beamline at the Shanghai Synchrotron Radiation Facility. The storage rings of the Shanghai Synchrotron Radiation Facility were operated at 3.5 GeV with a stable current of 200 mA. Using a Si (111) double-crystal monochromator, data collection was carried out in fluorescence mode using a Lytle detector. All spectra were collected under ambient conditions.

### Mechanical compression of persistent phosphors

Persistent phosphors were poured into an open mould (diameter, 7 mm). A pressure of 2 tons was applied to compress the powder for 20 s. A round disk of the powder was removed from the open mould for further characterization. The open mould (PMK-YB) and the tablet machine (PC-12S) were purchased from Jingtuo Instrument and Technology.

### Electronic trap depth of NaLuF<sub>4</sub>:Tb/Gd (15/*x* mol%; *x* = 0–35) nanocrystals

The depth of electronic traps was characterized by measuring temperature-dependent thermoluminescence spectra of the NaLuF<sub>4</sub>:Tb/Gd (15/*x* mol%; *x* = 0–35) nanocrystals using the initial rise analysis method<sup>35</sup>. In a typical procedure, materials were heated at a temperature of 550 K to completely release their trapped carriers using a cooling/heating stage (Linkam Scientific Instruments, HSF 600). Next, these samples were excited by an X-ray source for 5 min at a set temperature. Afterward, samples were heated to 550 K at a rate of 1 K s<sup>−1</sup>. Light output was measured using an Edinburgh FS5 spectrometer coupled with an optical fibre.

### Mechanical characterization

The stretchability of silicone rubber was measured with an electrical universal material testing machine (CMT4104, MTS Systems). Silicone rubber samples were cut into rectangles 50 mm in length, 10 mm in width and 1 mm in thickness.

### Fabrication of a flexible X-ray detector

In a typical experiment, SYLGARD 184 silicone elastomer base was premixed with the curing agent (10:1 by mass). Platinum-catalysed rubber elastomer was prepared by casting the commercial Ecoflex 30 (Smooth-On) mixture (part A and part B in 1:1 weight ratio). A cyclohexane solution of NaLuF<sub>4</sub>:Tb (15 mol%)@NaYF<sub>4</sub> nanocrystals with various concentrations was added to the resultant solution while stirring vigorously. The mixture was poured into a square acrylic plate (16 × 16 cm<sup>2</sup>) as a mould for thin-film fabrication. The resulting composites were degassed in a vacuum container to remove air bubbles. The mixture was finally heated at 80 °C for 4 h. After cooling to room temperature, the as-fabricated film (thickness, 1 mm) was peeled from the square acrylic template and used for X-ray imaging.

### Experimental setup for X-ray luminescence extension imaging

A charge-coupled device camera (Tucsen, FL-20BW) was coupled with AZURE-6515TH10M objective (AZURE Photonics) and fixed on a bracket (Olympus China) using a quasi-focus screw. A heating plate was placed under the flexible X-ray detector to stimulate radioluminescence afterglow after turning off X-rays.

### Digital X-ray imaging

In a typical procedure for X-ray imaging, the flexible X-ray detector was inserted into an electronic board or placed on its surface. A beam of X-ray source (P357, VJ Technologies) or miniature X-ray source (Amptek)

was applied to the electronic board with different amounts of X-ray exposure. After X-ray exposure, the flexible X-ray detector was placed on a metal plate and heated to 80 °C. Images were recorded using a digital camera (exposure time, 10 s) or a smartphone or an optical microscope.

### Three-dimensional projection of acquired X-ray images

A 3D model of a printed circuit board was constructed using Solidworks software. The recorded X-ray images were projected onto the surface of the 3D model.

### Calculation of electronic trap depth using the initial rise analysis method

Thermally stimulated luminescence was performed to investigate the electronic trap depth in the as-synthesized persistent luminescent nanomaterials. Using the initial analysis method, temperature-dependent luminescence spectra under different excitation temperatures were measured to calculate the distribution of trap depth. The equation for the first, second and general order afterglow curve can be expressed as:

$$I(T) = C \exp\left(-\frac{E_t}{kT}\right), \quad (1)$$

where *I* is the intensity of thermally stimulated luminescence, *C* is a constant, *E<sub>t</sub>* is the defect energy level, *k* is the Boltzmann constant and *T* is the temperature. When the equation was plotted in an Arrhenius kinetic process, the equation in (1) can be expressed as:

$$\ln I(T) = \ln C - \frac{E_t}{kT}. \quad (2)$$

Hence, the trap depth can be determined by the slope of the straight section on the low-temperature side:

$$E_t = -k \times 8.617 \times 10^{-2} \text{ eV}. \quad (3)$$

The glow curves of equation (1) are integrated to obtain the density of trapped electrons. The distribution of trap depth can be obtained by calculating the difference between each energy level.

### Density functional theory

DFT calculations were performed to determine the formation energies of defects and the corresponding ground-state electronic properties of both intrinsic and defective NaLuF<sub>4</sub> lattice with *P6<sub>3</sub>* space group. To calculate the transient formation energy of the anion Frenkel defect, DFT+U calculations were conducted using the CASTEP (Cambridge Serial Total Energy Package) source code<sup>36</sup>, and the on-site Coulomb energy of the spurious electron self-energy was corrected using self-consistent determined *U* parameters on the localized 4*f* orbitals of rare-earth elements. The norm-conserving pseudopotentials for Na, Tb, Lu and F atoms were generated using the OPIUM code in the Kleinman–Bylander projector form<sup>37</sup>. Note that nonlinear partial core correction and a scalar relativistic averaging scheme are used to treat the spin–orbital coupling effect. In particular, we treated the (4*f*, 5*s*, 5*p*, 5*d*, 6*s*) states as valence states of the Tb and Lu atoms. The time-dependent DFT calculation was performed with a two-electron-based Tamm–Dancoff approximation imported from our self-consistent corrected ground-state wave function. A full set of optical properties of systems was retrieved by calculating excitation energies and transition probabilities, revealing more precise locations of absorption peaks in the optical spectrum than Kohn–Sham excitation energies.

Concurrently, to estimate the location of impurity levels with respect to the bands of the NaLuF<sub>4</sub> host, the screened-exchange hybrid density functional HSE06 was used to calculate precise ground-state electronic structures with spin–orbit coupling effect<sup>38</sup>. Note that 12% of



the GGA-PBE functional is replaced by the Hartree–Fock exchange. These electronic calculations were performed within the framework of DFT implemented in the Vienna ab initio simulation package with the projector augmented wave method<sup>39</sup>.

## Finite element simulation

To investigate tensile strain (the first principal stress) on the silicone rubber film structure, the finite element simulations were performed using commercial FET software COMSOL (COMSOL LIC). Geometries were meshed using eight-node hexahedron elements. The Mooney–Rivlin model was used to capture the hyperelastic behaviour of the material. For the random point in elastomer, the equilibrium differential equation along the Cartesian axis  $(x, y, z)$  can be expressed as:

$$\begin{cases} \frac{\partial \sigma_x}{\partial x} + \frac{\partial \tau_{xy}}{\partial y} + \frac{\partial \tau_{xz}}{\partial z} + f_x = 0 \\ \frac{\partial \tau_{yx}}{\partial x} + \frac{\partial \sigma_y}{\partial y} + \frac{\partial \tau_{yz}}{\partial z} + f_y = 0, \\ \frac{\partial \tau_{zx}}{\partial x} + \frac{\partial \tau_{yz}}{\partial y} + \frac{\partial \sigma_z}{\partial z} + f_z = 0 \end{cases}$$

where  $f_x, f_y$  and  $f_z$  are the components of the vector of the stress per unit volume in the  $x, y$  and  $z$  directions.  $\tau$  and  $\sigma$  denote normal and shear stress, respectively. When slight displacement and deformation occur, if higher-order and nonlinear terms of the displacement derivative are omitted, the geometric equation in the Cartesian coordinate system  $x, y, z$  can be expressed as:

$$\begin{cases} \varepsilon_x = \frac{\partial u}{\partial x}, \gamma_{xy} = \frac{\partial u}{\partial y} + \frac{\partial v}{\partial x} \\ \varepsilon_y = \frac{\partial v}{\partial y}, \gamma_{yz} = \frac{\partial v}{\partial z} + \frac{\partial w}{\partial y}, \\ \varepsilon_z = \frac{\partial w}{\partial z}, \gamma_{xz} = \frac{\partial u}{\partial z} + \frac{\partial w}{\partial x} \end{cases}$$

where  $u, v$  and  $w$  represent displacement in the  $x, y$  and  $z$  directions, respectively. When large displacement and deformation occur, nonlinear terms of displacement derivatives are preserved, and the geometric equation in the Cartesian coordinate system  $x, y, z$  can be expressed as:

$$\begin{cases} \varepsilon_x = \frac{\partial u}{\partial x} + \frac{1}{2} \left[ \left( \frac{\partial u}{\partial x} \right)^2 + \left( \frac{\partial v}{\partial x} \right)^2 \right], \gamma_{xy} = \frac{\partial v}{\partial x} + \frac{\partial u}{\partial y} + \frac{\partial u}{\partial x} \frac{\partial u}{\partial y} + \frac{\partial v}{\partial x} \frac{\partial v}{\partial y} \\ \varepsilon_y = \frac{\partial v}{\partial y} + \frac{1}{2} \left[ \left( \frac{\partial v}{\partial y} \right)^2 + \left( \frac{\partial w}{\partial y} \right)^2 \right], \gamma_{yz} = \frac{\partial w}{\partial y} + \frac{\partial v}{\partial z} + \frac{\partial v}{\partial y} \frac{\partial v}{\partial z} + \frac{\partial w}{\partial y} \frac{\partial w}{\partial z} \\ \varepsilon_z = \frac{\partial w}{\partial z} + \frac{1}{2} \left[ \left( \frac{\partial w}{\partial z} \right)^2 + \left( \frac{\partial u}{\partial z} \right)^2 \right], \gamma_{xz} = \frac{\partial u}{\partial z} + \frac{\partial w}{\partial x} + \frac{\partial w}{\partial z} \frac{\partial w}{\partial x} + \frac{\partial u}{\partial z} \frac{\partial u}{\partial x} \end{cases}$$

The physical equation can be expressed as:

$$\sigma = K^T \sigma_1 = K^T D \varepsilon_1 = K^T D K \varepsilon = D \varepsilon,$$

where  $D$  is the elastic matrix and  $\varepsilon$  is the strain matrix.  $D, \sigma_1$  and  $\varepsilon_1$  refer to the element stiffness matrix, the element stress matrix and the element strain matrix, respectively.

Assuming that the internal force per unit area of the elastic body on the boundary is  $T_x, T_y, T_z$ , and the area force acting on the unit area of the known elastomer on the boundary  $S_o$  (force boundary) is  $\bar{T}_x, \bar{T}_y, \bar{T}_z$ . According to the plane conditions:

$$T_x = \bar{T}_x, T_y = \bar{T}_y, T_z = \bar{T}_z.$$

Supposing that the outer normal of the boundary is  $N$  and the cosine of its direction is  $n_x, n_y, n_z$ , the internal force of the elastomer on the boundary can be determined by the following formula:

$$\begin{cases} T_x = n_x \sigma_x + n_y \tau_{xy} + n_z \tau_{xz} \\ T_y = n_x \tau_{xy} + n_y \sigma_y + n_z \tau_{yz} \\ T_z = n_x \tau_{xz} + n_y \tau_{yz} + n_z \sigma_z \end{cases}$$

or

$$\{T\} = n\{\sigma\}.$$

Among them:

$$n = \begin{bmatrix} n_x & 0 & 0 & n_y & 0 & n_z \\ 0 & n_y & 0 & n_x & n_z & 0 \\ 0 & 0 & n_z & 0 & n_y & n_x \end{bmatrix}.$$

The displacement of the elastomer on  $S_u$  is  $\bar{u}, \bar{v}, \bar{w}$ , hence:

$$u = \bar{u}, v = \bar{v}, w = \bar{w},$$

where  $S_u$  is the boundary conditions of the displacement.

## Data availability

The data that support the findings of this study are available from the corresponding authors upon reasonable request.

35. Van den Eeckhout, K., Bos, A. J. J., Poelman, D. & Smet, P. F. Revealing trap depth distributions in persistent phosphors. *Phys. Rev. B* **87**, 045126 (2013).
36. Huang, B. Doping of RE ions in the 2D ZnO layered system to achieve low-dimensional upconverted persistent luminescence based on asymmetric doping in ZnO systems. *Phys. Chem. Chem. Phys.* **19**, 12683–12711 (2017).
37. Rappe, A. M., Rabe, K. M., Kaxiras, E. & Joannopoulos, J. D. Optimized pseudopotentials. *Phys. Rev. B* **41**, 1227–1230 (1990).
38. Heyd, J., Scuseria, G. E. & Ernzerhof, M. Hybrid functionals based on a screened Coulomb potential. *J. Chem. Phys.* **118**, 8207–8215 (2003).
39. Kresse, G. & Furthmüller, J. Efficiency of ab-initio total energy calculations for metals and semiconductors using a plane-wave basis set. *Comput. Mater. Sci.* **6**, 15–50 (1996).

**Acknowledgements** We thank L. Ma, Y. Huang, X. Wang and B. Hou for technical assistance. This work is supported by the National Key and Program of China (grant number 2018YFA0902600), the National Natural Science Foundation of China (grant numbers 21635002, 21771135, 21871071 and 21771156), the Early Career Scheme fund (grant number PolyU 253026/16P) from the Research Grant Council in Hong Kong, Research Institute for Smart Energy of the Hong Kong Polytechnic University, Agency for Science, Technology and Research (grant numbers A1883c0011 and A1983c0038), NUS NanoNash Programme (NUHSRO/2020/002/NanoNash/LOA and R143000B43114) and National Research Foundation, the Prime Minister's Office of Singapore under its NRF Investigatorship Programme (award number NRF-NRFIO5-2019-0003).

**Author contributions** X.O. and H.Y. initiated the project. Q.C. and X.L. conceived the concept of X-ray luminescence extension imaging. X.L., H.Y. and Q.C. supervised the project and organized the collaboration. X.O., X.L., H.Y. and Q.C. designed the experiments. X.O., Q.W., X.C., Z.H. and J.Z. performed nanocrystal synthesis. X.O., Q.W., J.Z. and L.X. performed luminescence measurements and X-ray imaging. X.O., Z.Y. and H.B. performed flexible X-ray imaging. X.Q. and B.H. carried out theoretical calculations. J.L., H.B. and Y.W. fabricated PDMS moulds and measured low-temperature scintillation spectra. X.O., H.Y., Q.C. and X.L. wrote the manuscript. All authors discussed the results and commented on the manuscript.

**Competing interests** The authors declare no competing interests.

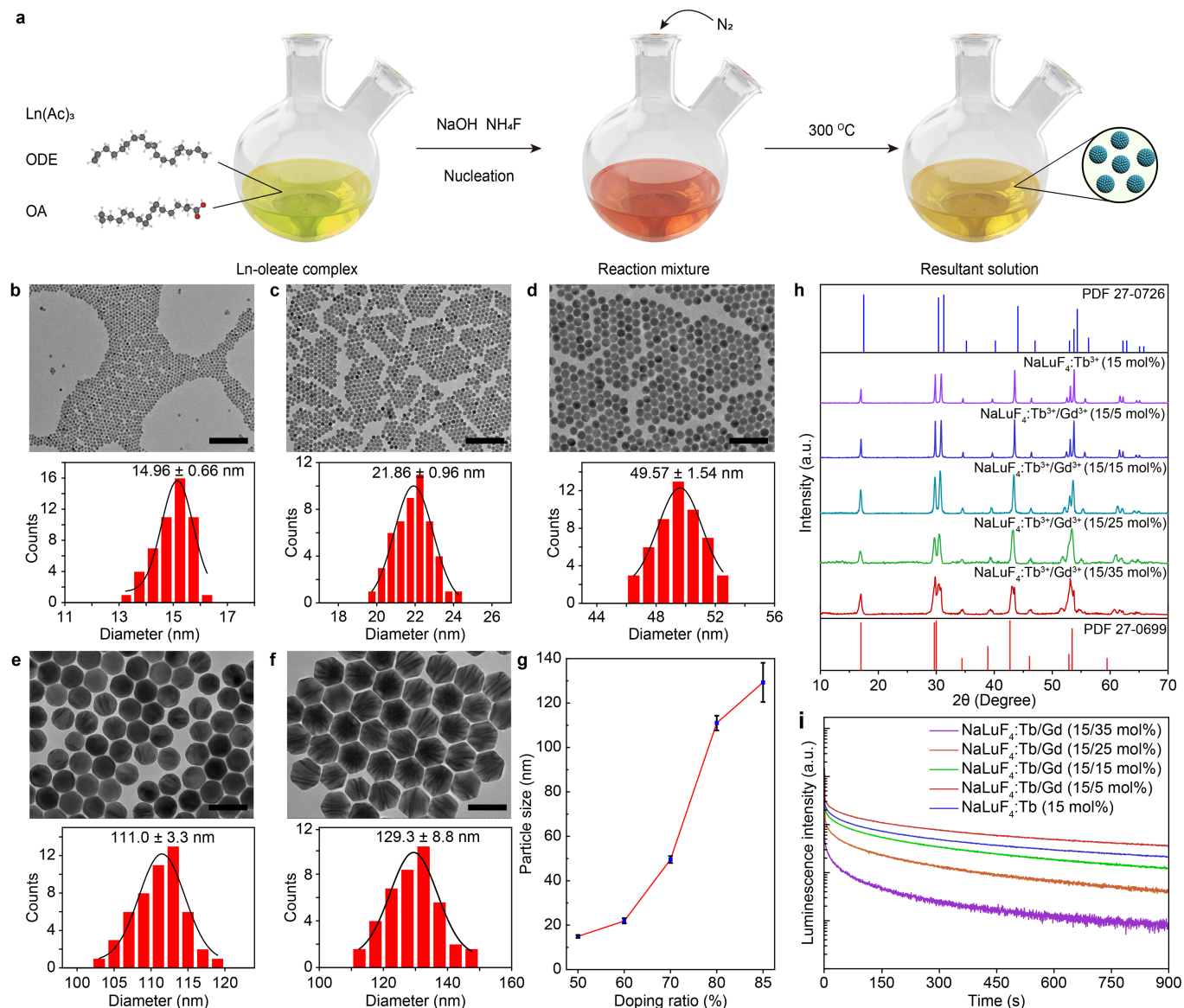
## Additional information

**Supplementary information** The online version contains supplementary material available at <https://doi.org/10.1038/s41586-021-03251-6>.

**Correspondence and requests for materials** should be addressed to Q.C., H.Y. or X.L.

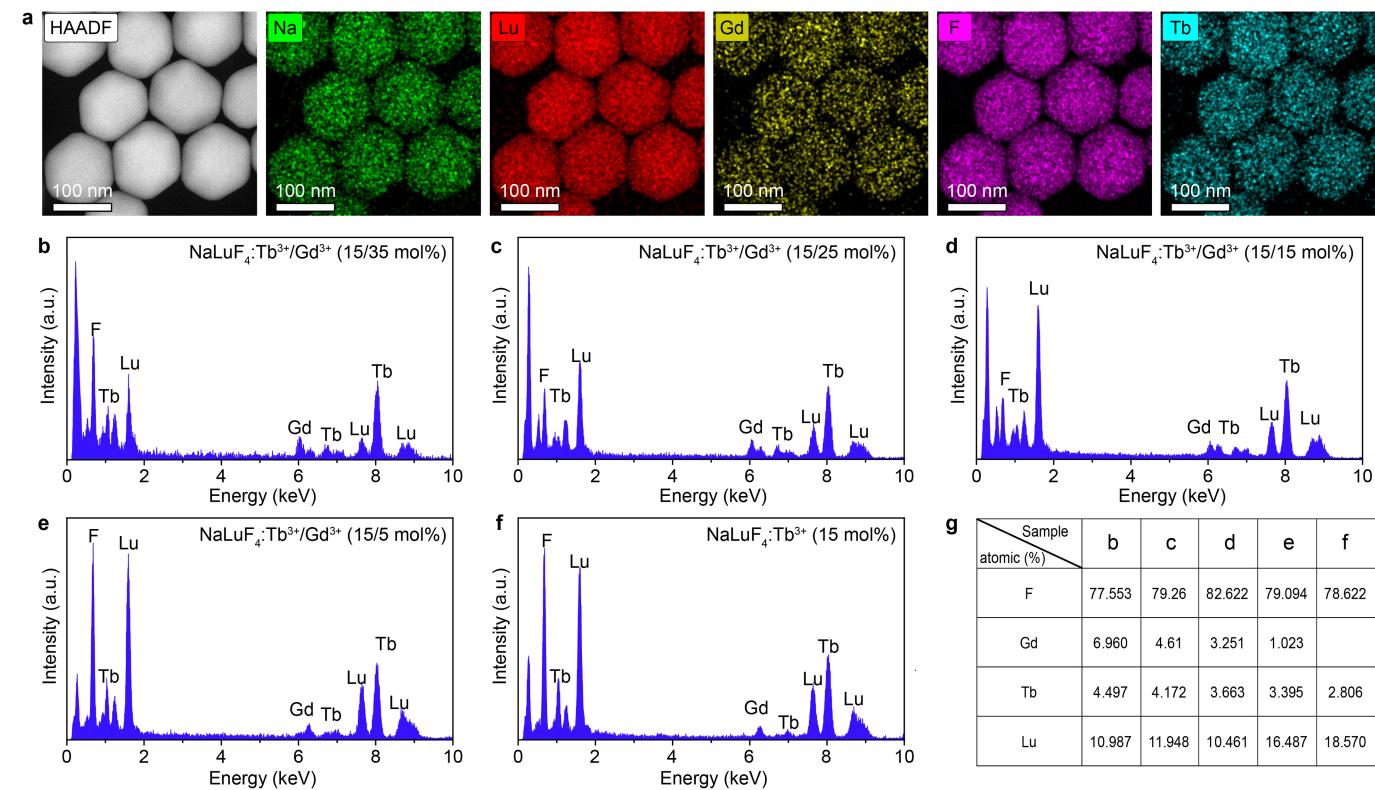
**Peer review information** Nature thanks Christophe Dujardin, Oscar Malta and the other, anonymous, reviewer(s) for their contribution to the peer review of this work.

**Reprints and permissions information** is available at <http://www.nature.com/reprints>.



**Extended Data Fig. 1 | Synthesis and characterization of Tb<sup>3+</sup>-doped nanocrystals.** **a**, Schematic for the synthesis of NaLuF<sub>4</sub>:Ln/Gd (Ln = Pr<sup>3+</sup>, Sm<sup>3+</sup>, Ho<sup>3+</sup>, Er<sup>3+</sup>, Tb<sup>3+</sup>, Dy<sup>3+</sup>, Tm<sup>3+</sup> and Nd<sup>3+</sup>) nanocrystals. In a typical procedure, lanthanide acetate salts (Ln(Ac)<sub>3</sub>·xH<sub>2</sub>O) were added to a flask containing OA and ODE. The mixture was heated at 150 °C to form lanthanide-oleate coordination complexes. Nucleation of NaLuF<sub>4</sub>:Ln/Gd nanocrystals was triggered by injecting a methanol solution of NaOH and NH<sub>4</sub>F. Subsequently, the reaction solution was heated at 300 °C for 1 h. The final product was precipitated with ethanol. OA was used as a surface ligand to control the particle size and stabilize as-synthesized nanocrystals. **b–f**, Low-resolution TEM images of as-synthesized hexagonal-phase nanocrystals (top) and corresponding size

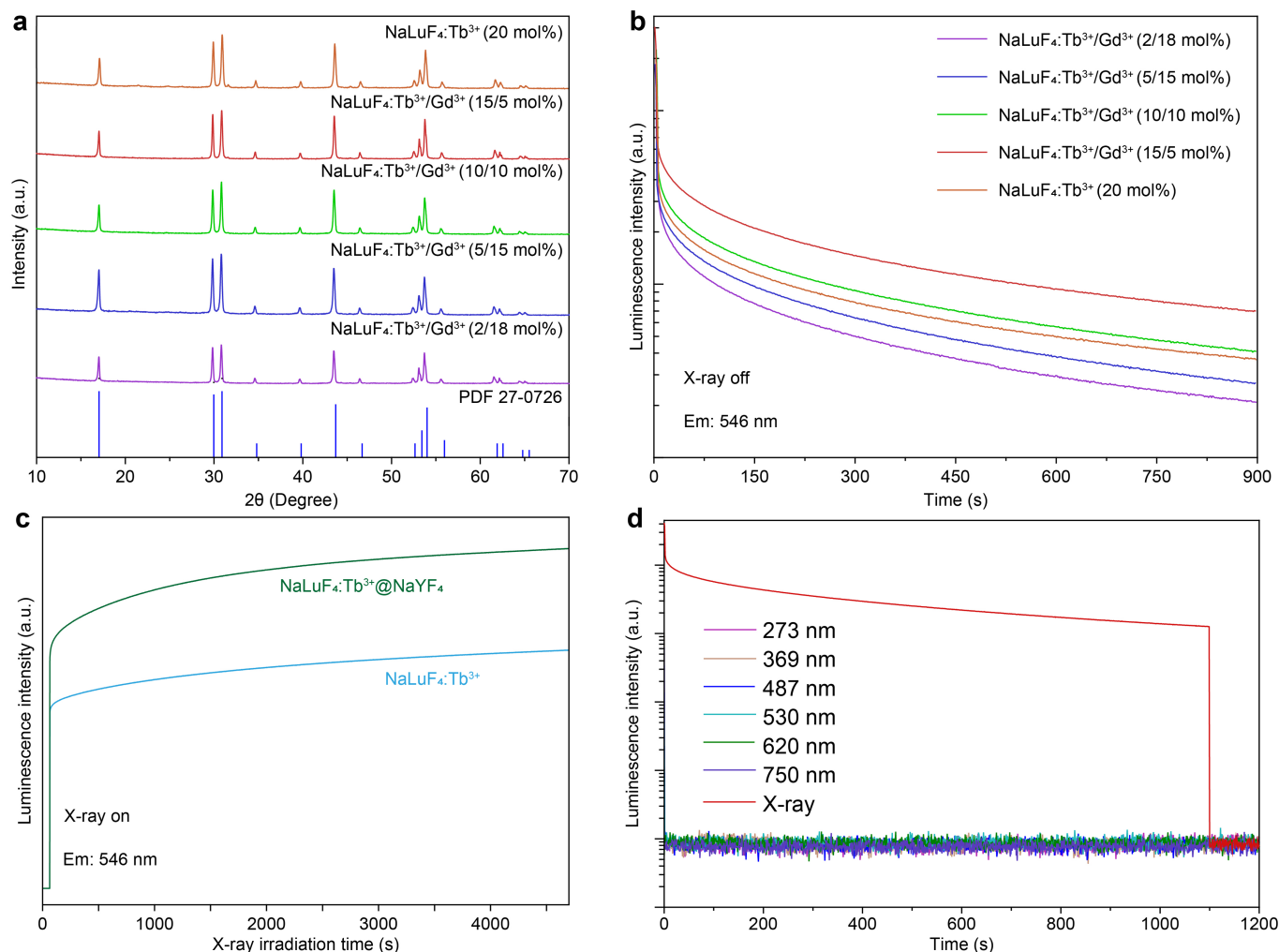
distributions (bottom). These samples are NaLuF<sub>4</sub>:Tb/Gd (15/35 mol%) (**b**), NaLuF<sub>4</sub>:Tb/Gd (15/25 mol%) (**c**), NaLuF<sub>4</sub>:Tb/Gd (15/15 mol%) (**d**), NaLuF<sub>4</sub>:Tb/Gd (15/5 mol%) (**e**) and NaLuF<sub>4</sub>:Tb (15 mol%) (**f**). Scale bars, 200 nm. **g**, Particle size as a function of the lutetium doping ratio. **h**, Powder X-ray diffraction patterns for NaLuF<sub>4</sub>:Tb/Gd (15/x mol%; x = 0–35) nanocrystals. All peaks are consistent with the hexagonal-phase NaLuF<sub>4</sub> structure (Joint Committee on Powder Diffraction Standards (PDF) file number 27-0726). **i**, Corresponding persistent radioluminescence decay curves of NaLuF<sub>4</sub>:Tb/Gd (15/x mol%; x = 0–35) nanocrystals monitored at 546 nm as a function of time. Spectra were obtained after X-ray excitation at a power density of 278 μGy s<sup>-1</sup> for 5 min at room temperature (298 K).



**Extended Data Fig. 2 | Chemical composition analysis of Tb<sup>3+</sup>-doped fluoride nanocrystals. a**, Energy-dispersive X-ray element mapping of as-prepared NaLuF<sub>4</sub>:Tb/Gd (15/5 mol%) nanocrystals (Na, green; Lu, red; Gd, yellow; F, purple; Tb, green blue). **b–f**, EDX spectra of NaLuF<sub>4</sub>:Tb/Gd

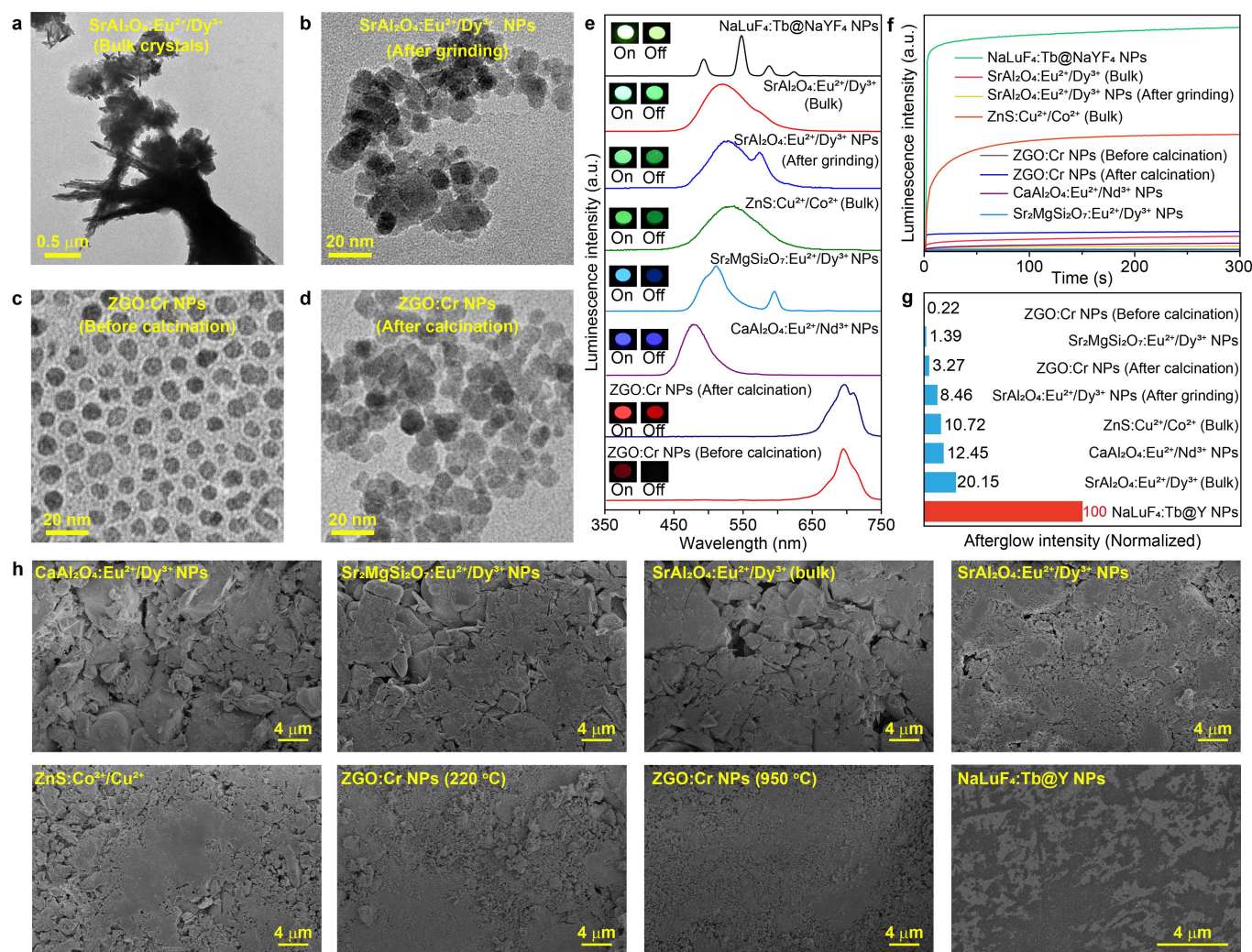
(15/35 mol%) (**b**), NaLuF<sub>4</sub>:Tb/Gd (15/25 mol%) (**c**), NaLuF<sub>4</sub>:Tb/Gd (15/15 mol%) (**d**), NaLuF<sub>4</sub>:Tb/Gd (15/5 mol%) (**e**) and NaLuF<sub>4</sub>:Tb (15 mol%) (**f**) nanocrystals. **g**, Corresponding stoichiometric composition of NaLuF<sub>4</sub>:Tb/Gd (15/*x* mol%; *x* = 0–35) nanocrystals.





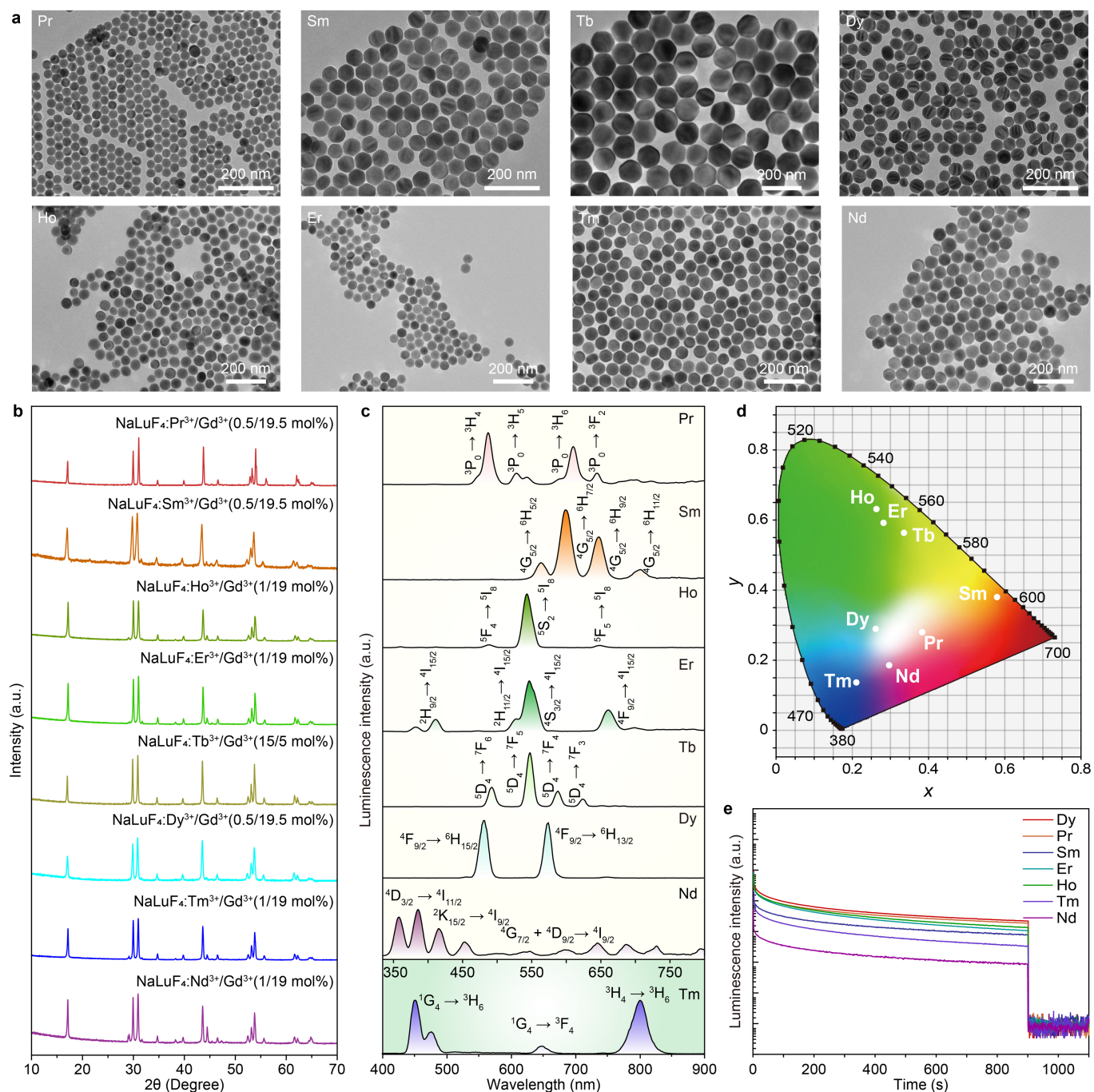
**Extended Data Fig. 3 | Afterglow characterizations of the  $\text{Tb}^{3+}$ -doped nanocrystals.** **a**, Powder X-ray diffraction patterns of  $\text{NaLuF}_4:\text{Tb}/\text{Gd}$  ( $x/(20-x)$  mol%;  $x=2-20$ ) nanocrystals, showing that all peaks are consistent with hexagonal-phase  $\text{NaLuF}_4$  (Joint Committee on Powder Diffraction Standards file number 27-0726). **b**, Radioluminescence decay curves of  $\text{NaLuF}_4:\text{Tb}^{3+}/\text{Gd}^{3+}$  ( $x/(20-x)$  mol%;  $x=2-20$ ) nanocrystals monitored at 546 nm after cessation of X-rays (dose rate,  $278 \mu\text{Gy s}^{-1}$ ; excitation time, 300 s; temperature, 298 K).

**c**, Radioluminescence intensities, monitored at 546 nm as a function of time, of as-synthesized  $\text{NaLuF}_4:\text{Tb}$  (15 mol%) and  $\text{NaLuF}_4:\text{Tb}$  (15 mol%)@ $\text{NaYF}_4$  nanocrystals upon continuous X-ray irradiation. **d**, Luminescent decay profiles of  $\text{NaLuF}_4:\text{Tb}$  (15 mol%)@ $\text{NaYF}_4$  nanocrystals. The luminescence intensity was monitored at 546 nm as a function of time, recorded upon turning off X-rays or ultraviolet-visible excitation at 273, 369, 487, 530, 620 and 750 nm for 5 min, respectively. All measurements were performed at room temperature.



**Extended Data Fig. 4 | Morphology and radioluminescent afterglow performance of various persistent phosphors upon X-ray excitation.** **a-d**, Representative TEM images of  $\text{SrAl}_2\text{O}_4:\text{Eu}^{2+}/\text{Dy}^{3+}$  powder (**a**), mechanically grounded  $\text{SrAl}_2\text{O}_4:\text{Eu}^{2+}/\text{Dy}^{3+}$  nanoparticles (**b**), ZnGa<sub>2</sub>O<sub>4</sub>:Cr<sup>3+</sup> (ZGO:Cr) nanoparticles prepared by hydrothermal synthesis at 220 °C (**c**) and ZGO:Cr nanoparticles calcinated at 950 °C (**d**). **e**, Radioluminescence spectra of NaLuF<sub>4</sub>:Tb(15 mol%)/NaYF<sub>4</sub> nanoparticles,  $\text{SrAl}_2\text{O}_4:\text{Eu}^{2+}/\text{Dy}^{3+}$  bulk powder, ZnS:Cu<sup>2+</sup>/Co<sup>2+</sup> bulk powder,  $\text{SrAl}_2\text{O}_4:\text{Eu}^{2+}/\text{Dy}^{3+}$  nanoparticles (after grinding), ZnGa<sub>1.995</sub>O<sub>4</sub>:Cr<sub>0.005</sub> (ZGO:Cr) nanoparticles (before and after calcination),

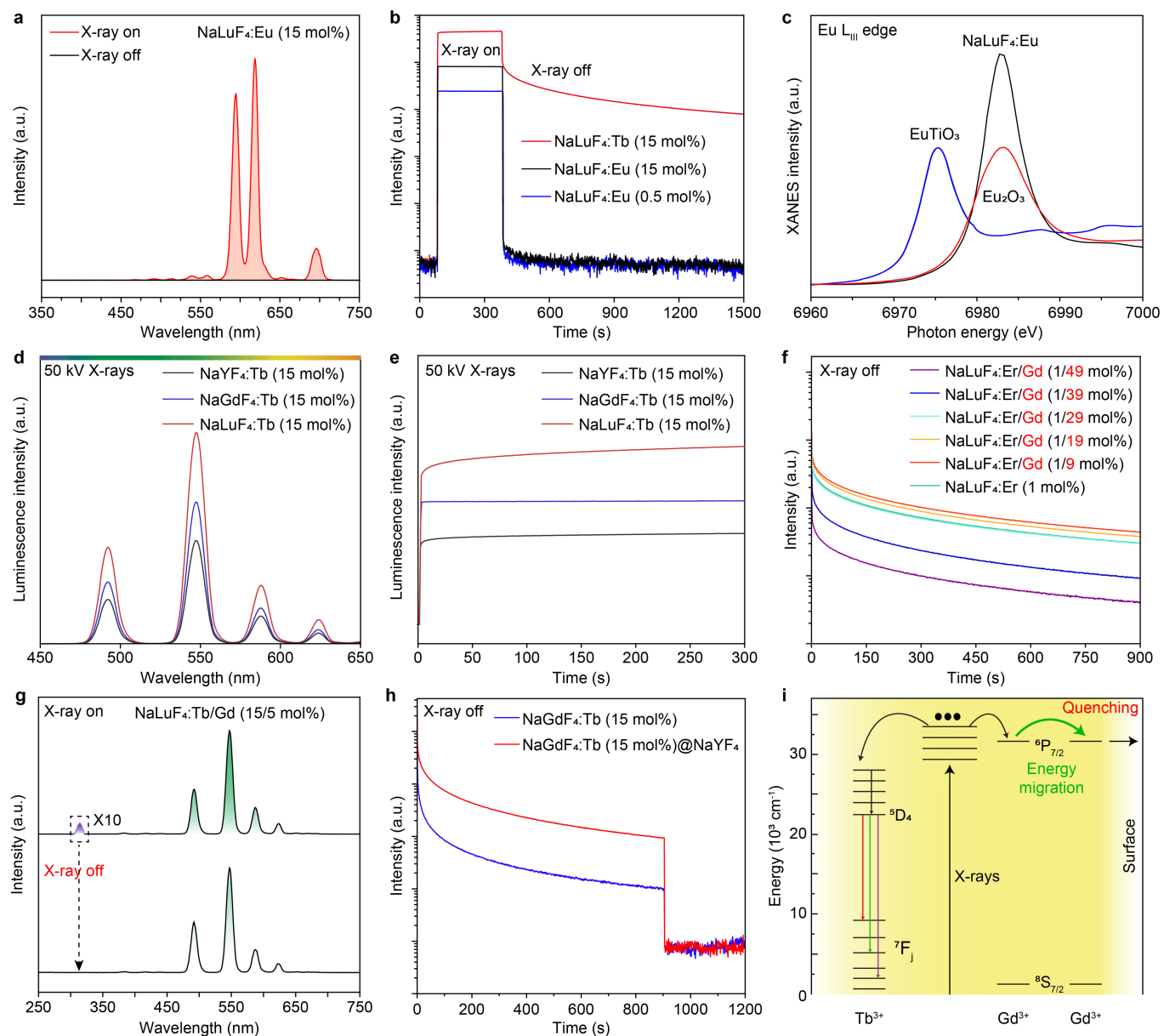
$\text{CaAl}_2\text{O}_4:\text{Eu}^{2+}/\text{Nd}^{3+}$  nanoparticles (after grinding) and  $\text{Sr}_2\text{MgSi}_2\text{O}_7:\text{Eu}^{2+}/\text{Dy}^{3+}$  nanoparticles (after grinding). Insets show corresponding photographs of the samples under X-ray excitation. **f**, Radioluminescence intensity profiles of various persistent luminescent materials upon continuous X-ray irradiation as a function of time (accelerating voltage, 50 kV; temperature, 298 K). **g**, Comparison of afterglow intensities of various persistent phosphors. Afterglow intensities were recorded after cessation of X-rays, following 300 s of X-ray excitation. **h**, Corresponding SEM images of compressed samples. All samples were prepared by a tablet machine without the PDMS matrix.



**Extended Data Fig. 5 | Characterization of persistent luminescent nanocrystals doped with different lanthanide activators.** **a**, TEM images of NaLuF<sub>4</sub>:Pr/Gd (0.5/19.5 mol%), NaLuF<sub>4</sub>:Sm/Gd (0.5/19.5 mol%), NaLuF<sub>4</sub>:Ho/Gd (1/19 mol%), NaLuF<sub>4</sub>:Er/Gd (1/19 mol%), NaLuF<sub>4</sub>:Tb/Gd (15/5 mol%), NaLuF<sub>4</sub>:Dy/Gd (0.5/19.5 mol%), NaLuF<sub>4</sub>:Tm/Gd (1/19 mol%) and NaLuF<sub>4</sub>:Nd/Gd (1/19 mol%) nanocrystals. All peaks are indexed in accordance with the hexagonal-phase NaLuF<sub>4</sub> structure (Joint Committee on Powder Diffraction Standards file number 27-0726). **b**, Powder X-ray diffraction patterns of NaLuF<sub>4</sub>:Ln/Gd (Ln = Pr<sup>3+</sup>, Sm<sup>3+</sup>, Ho<sup>3+</sup>, Er<sup>3+</sup>, Tb<sup>3+</sup>, Dy<sup>3+</sup>, Tm<sup>3+</sup> and Nd<sup>3+</sup>) nanocrystals. All peaks are indexed in accordance with the hexagonal-phase NaLuF<sub>4</sub> structure (Joint Committee on Powder Diffraction Standards file number 27-0726). **c**, Room-temperature afterglow spectra of NaLuF<sub>4</sub>:Pr/Gd (0.5/19.5 mol%), NaLuF<sub>4</sub>:Sm/Gd

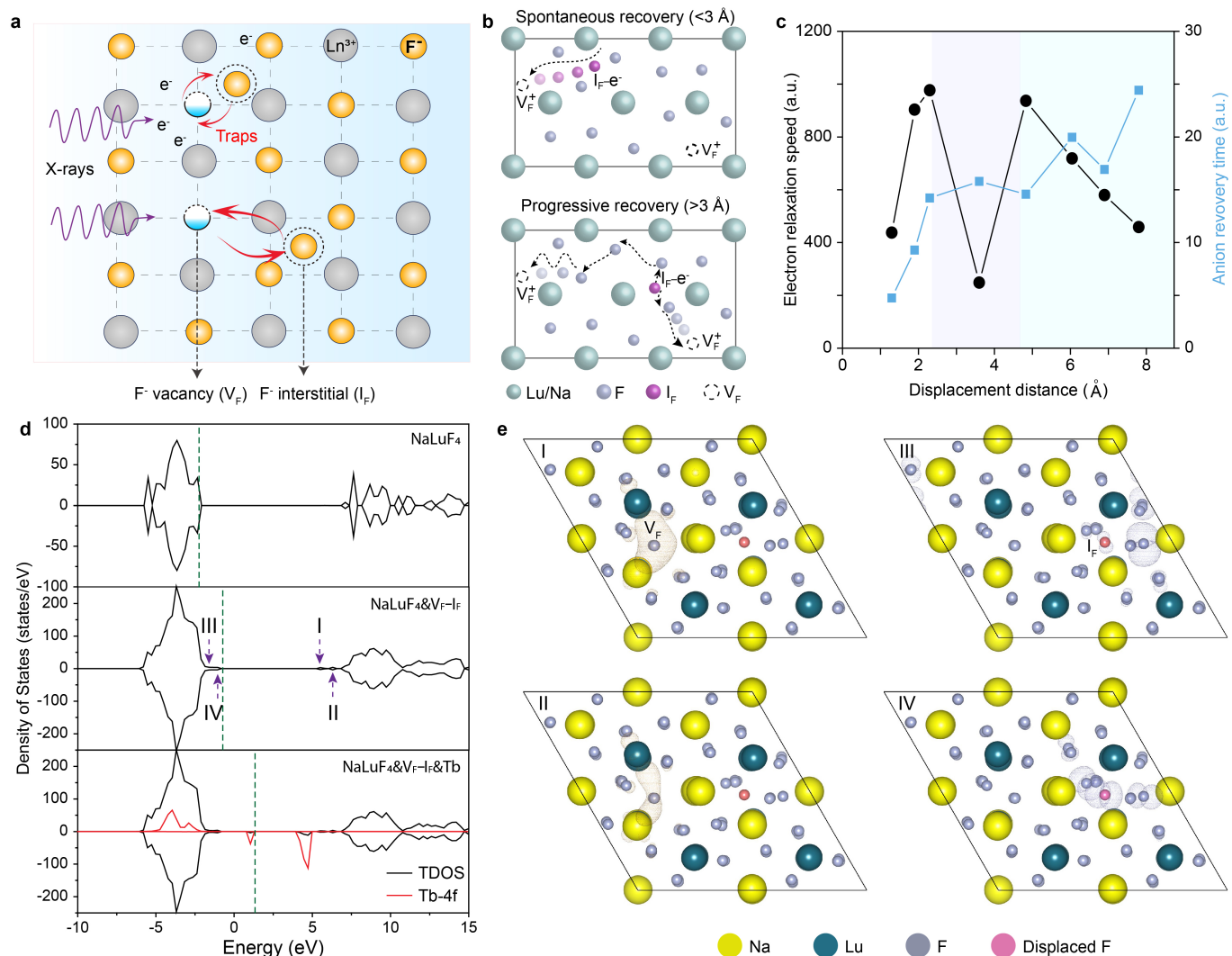
(0.5/19.5 mol%), NaLuF<sub>4</sub>:Ho/Gd (1/19 mol%), NaLuF<sub>4</sub>:Er/Gd (1/19 mol%), NaLuF<sub>4</sub>:Tb/Gd (15/5 mol%), NaLuF<sub>4</sub>:Dy/Gd (0.5/19.5 mol%), NaLuF<sub>4</sub>:Tm/Gd (1/19 mol%) and NaLuF<sub>4</sub>:Nd/Gd (1/19 mol%) nanocrystals. All spectra were recorded after turning off X-rays (dose rate, 278 μGy s<sup>-1</sup>; excitation time, 300 s). **d**, Corresponding commission Internationale de l'Éclairage chromaticity coordinates of persistent luminescence. **e**, Room-temperature afterglow decay curves of NaLuF<sub>4</sub>:Ln/Gd (Ln = Pr<sup>3+</sup>, Sm<sup>3+</sup>, Ho<sup>3+</sup>, Er<sup>3+</sup>, Dy<sup>3+</sup>, Tm<sup>3+</sup> and Nd<sup>3+</sup>) nanocrystals monitored at 606, 594, 542, 543, 573, 453 and 385 nm, respectively (dose rate, 278 μGy s<sup>-1</sup>; excitation time, 300 s).





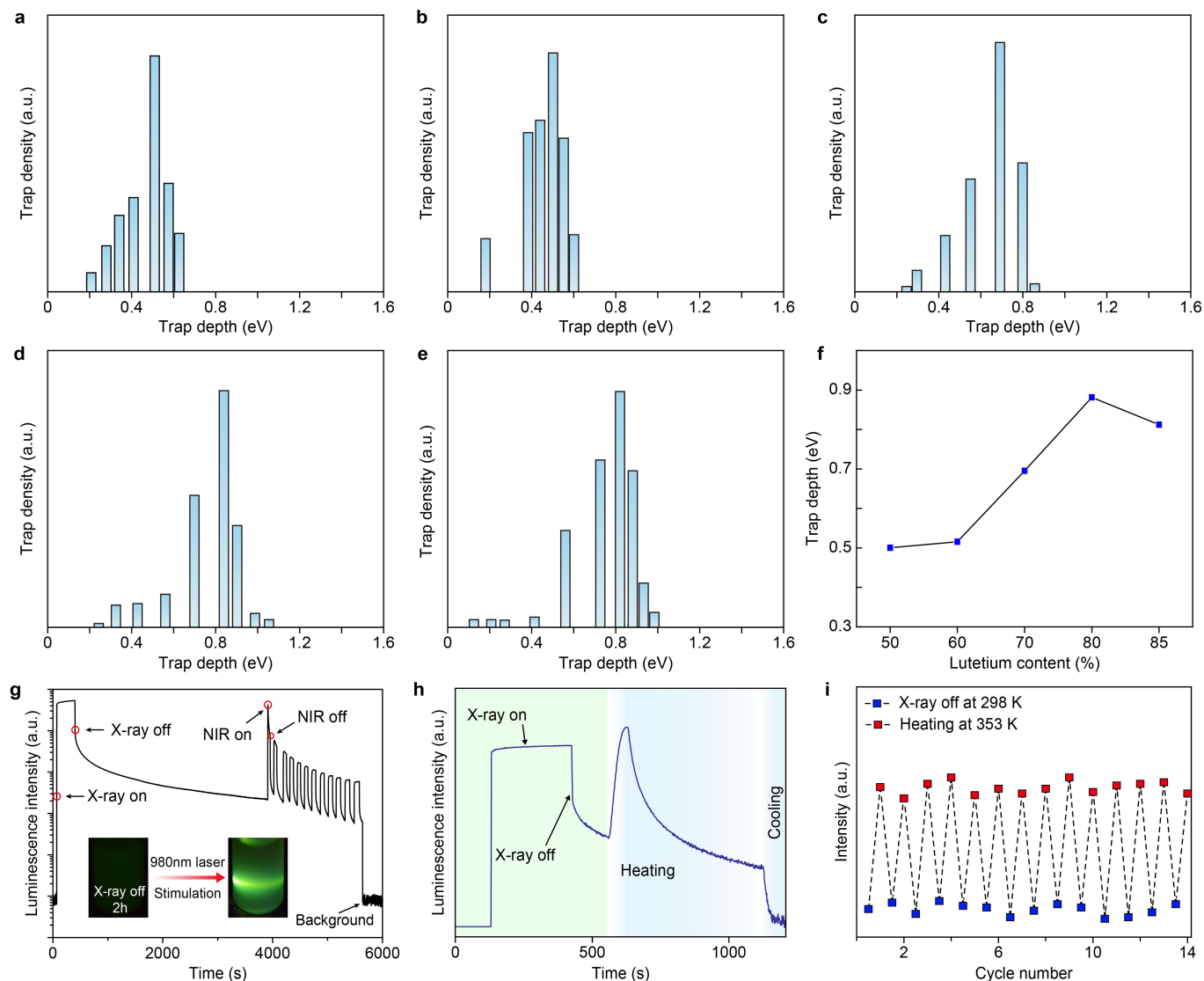
**Extended Data Fig. 6 | Physical investigation of X-ray-induced luminescence on lanthanide-doped fluoride nanocrystals.** **a**, Emission spectra of NaLuF<sub>4</sub>:Eu (15 mol%) nanocrystals with and without X-ray irradiation. **b**, Luminescence intensity of NaLuF<sub>4</sub>:Eu and NaLuF<sub>4</sub>:Tb nanocrystals as a function of time upon switching on/off X-rays. **c**, X-ray absorption near-edge structure (XANES) spectra of Tb L<sub>III</sub>-edge recorded for NaLuF<sub>4</sub>:Eu (15 mol%) nanocrystals and Eu<sub>2</sub>O<sub>3</sub> and EuTiO<sub>3</sub> references. **d**, Room-temperature emission spectra of NaYF<sub>4</sub>:Tb (15 mol%), NaGdF<sub>4</sub>:Tb (15 mol%), and NaLuF<sub>4</sub>:Tb (15 mol%) nanocrystals. **e**, X-ray-induced luminescence intensity of NaYF<sub>4</sub>:Tb (15 mol%), NaGdF<sub>4</sub>:Tb (15 mol%) and NaLuF<sub>4</sub>:Tb (15 mol%), monitored at 546 nm. All

samples were excited with X-ray irradiation at 50 kV (dose rate, 278  $\mu\text{Gy s}^{-1}$ ; temperature, 298 K). **f**, Luminescence decay curves of NaLuF<sub>4</sub>:Er/Gd (1/x mol%;  $x = 0-49$ ) nanocrystals after X-ray excitation is ceased. **g**, Emission spectra of NaLuF<sub>4</sub>:Tb/Gd (15/5 mol%) nanocrystals with and without X-ray irradiation, showing energy migration from Gd<sup>3+</sup> to Tb<sup>3+</sup>. **h**, Luminescence decay curves of the NaGdF<sub>4</sub>:Tb (15 mol%) core and NaGdF<sub>4</sub>:Tb(15 mol%)@NaYF<sub>4</sub> core-shell nanoparticles after cessation of X-rays. **i**, Schematic of NaGdF<sub>4</sub>:Tb crystal lattice and the energy level diagram of Gd<sup>3+</sup> and Tb<sup>3+</sup>. The excitation energy dissipates non-radiatively to quenching sites through energy migration.



**Extended Data Fig. 7 | Calculated electronic structures of  $\text{NaLuF}_4$ -based systems.** **a**, Schematic illustrating creation of Frenkel-related trap states in  $\text{NaLuF}_4$  crystal lattices upon high-energy X-ray irradiation. Small fluoride ions ( $\text{F}^-$ ) are then displaced from lattice to interstitial sites. This leads to many fluoride vacancies ( $V_F$ ) and interstitials ( $I_F$ ), along with trapping of energetic electrons ( $e^-$ ) at anion defects. **b**, Structural configuration of closely and distantly paired defects in the  $\text{NaLuF}_4$  lattice. Fluorine atoms are ejected from their original lattice sites to interstitial sites upon X-ray irradiation, followed by either spontaneous or stimulated self-recovery. **c**, Calculated electron and

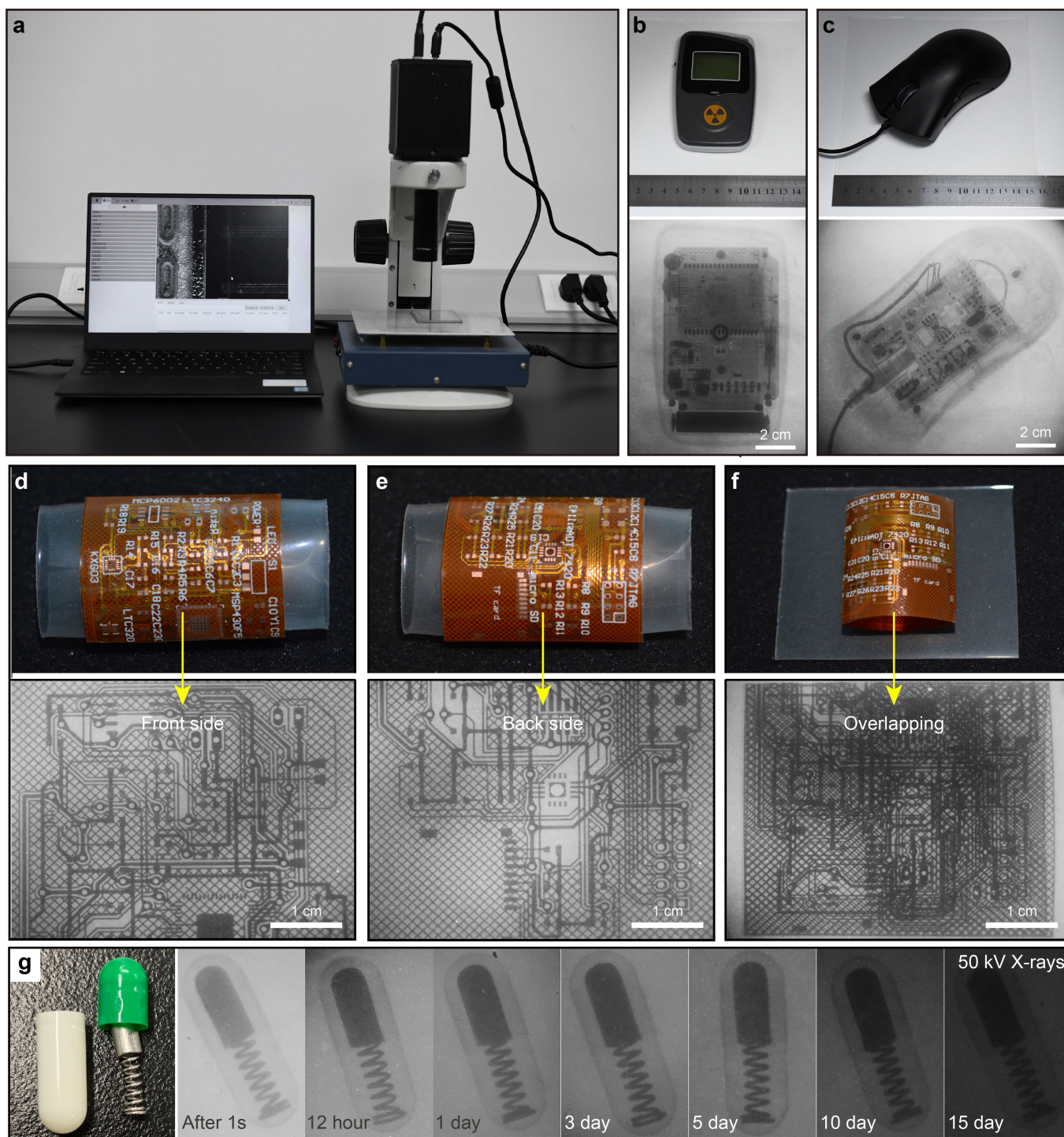
atom relaxation speed of defect pairs featuring different separation distances. **d**, Density of states of pristine  $\beta\text{-NaLuF}_4$  (top),  $V_F\text{-}I_F$ -contained  $\beta\text{-NaLuF}_4$  (middle) and  $V_F\text{-}I_F$ -contained  $\beta\text{-NaLuF}_4\text{:Tb}$  (bottom). Green dashed lines indicate the position of Fermi levels. Localized states due to F displacement are marked with arrows. Note that the values of the 4f-resolved density of states are scaled up (tenfold) for comparison purposes. **e**, The corresponding spatial distribution of partial charge densities of  $V_F$ - and  $I_F$ -induced localized states within the bandgap. Light purple and orange iso-surfaces are used for occupied and unoccupied localized states, respectively.



**Extended Data Fig. 8 | Characterization of electronic trap depth in NaLuF<sub>4</sub>:Tb/Gd (15/*x* mol%; *x* = 0–35) nanocrystals.** **a–e**, Density distribution of electronic trap depths in NaLuF<sub>4</sub>:Tb<sup>3+</sup>/Gd<sup>3+</sup> (15/35 mol%) (**a**), NaLuF<sub>4</sub>:Tb/Gd (15/25 mol%) (**b**), NaLuF<sub>4</sub>:Tb/Gd (15/15 mol%) (**c**), NaLuF<sub>4</sub>:Tb/Gd (15/5 mol%) (**d**) and NaLuF<sub>4</sub>:Tb (15 mol%) (**e**) nanocrystals. **f**, Measured electronic trap depth of Tb<sup>3+</sup>-doped nanocrystals as a function of the doping ratio of lutetium in the material host. Data were calculated from the measured results of **a–e**. **g**, Luminescence profile of NaLuF<sub>4</sub>:Tb(15 mol%)@NaYF<sub>4</sub> nanocrystals under

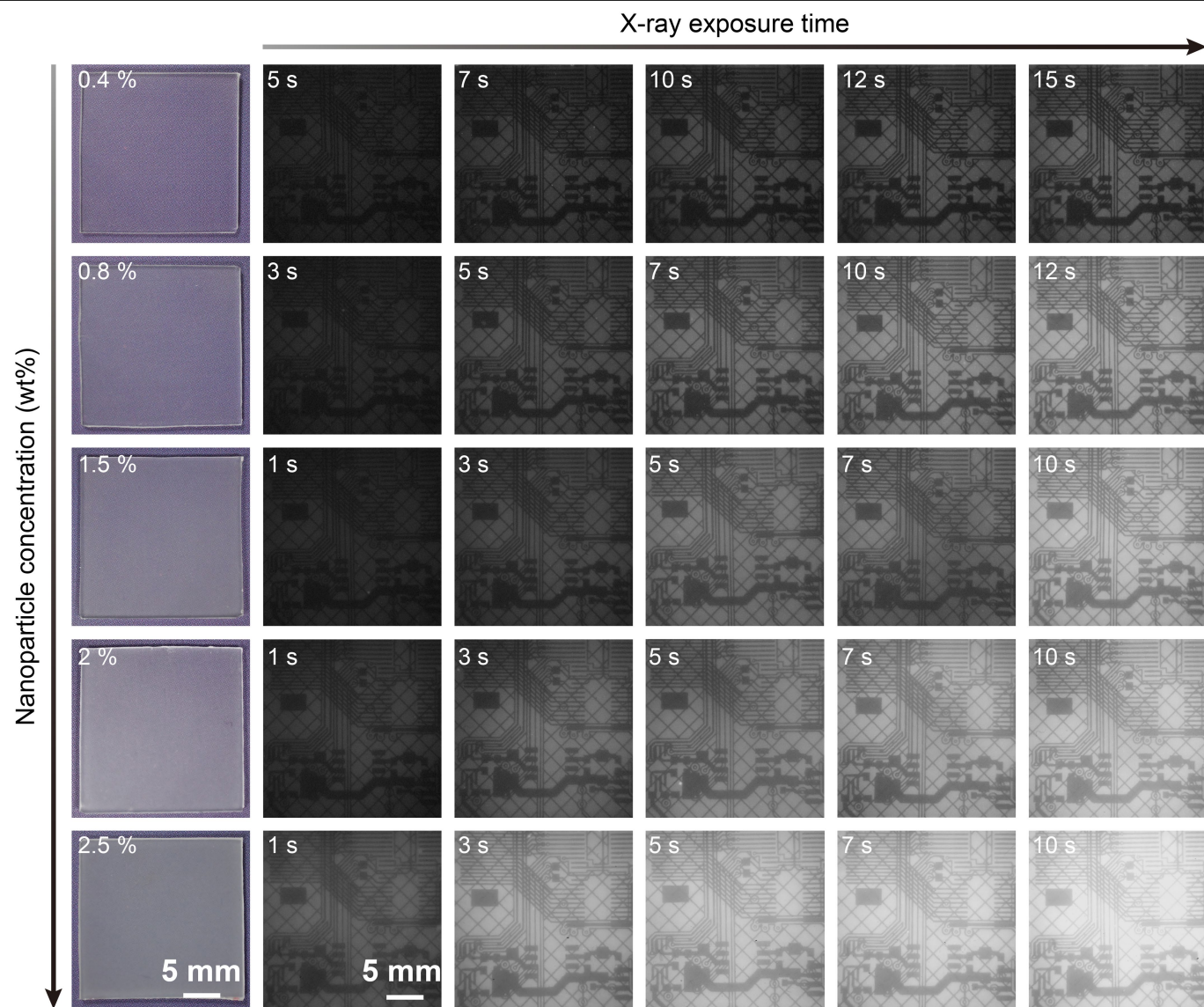
X-ray and after cessation of excitation, followed by cycled near-infrared stimulation with a 980-nm laser. **h**, Radioluminescence intensity of nanocrystals under repeated X-ray irradiation and thermal stimulation. Samples were excited with an X-ray source at 50 kV for 300 s. Radioluminescent afterglow decays quickly upon heating. **i**, Recycling performance evaluation of NaLuF<sub>4</sub>:Tb(15 mol%)@NaYF<sub>4</sub> nanocrystals under X-ray irradiation and heating at 80 °C for 14 cycles.





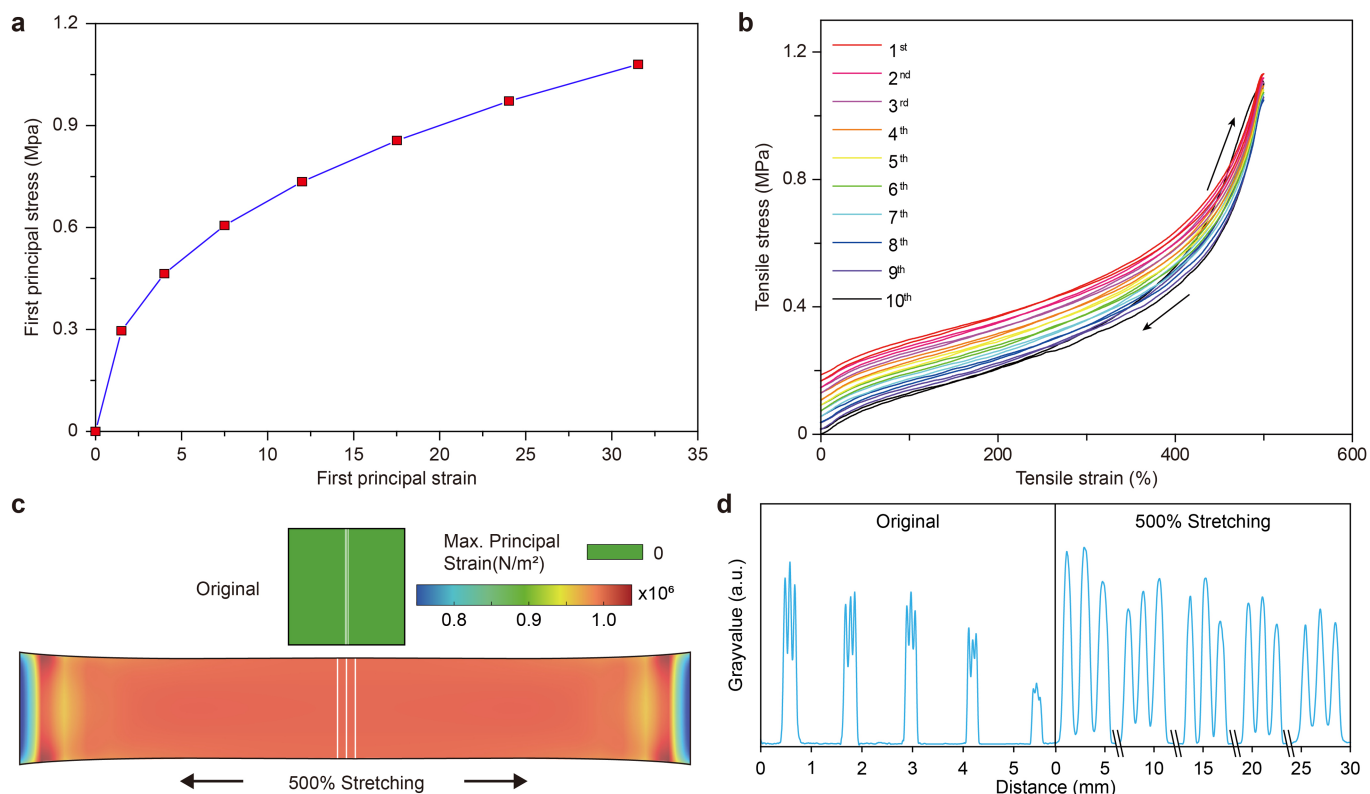
**Extended Data Fig. 9 | Xr-LEI based on persistent radioluminescent nanocrystals.** **a**, Schematic showing the microscopy setup for X-ray imaging. **b, c**, Bright-field photos (top) and X-ray images (bottom) of an X-ray dosimeter (**b**) and a computer mouse (**c**). **d–f**, Bright-field photos (top) and X-ray images (bottom) of a 3D electronic circuit board, conforming and adhering to the X-ray

detector (**d, e**) or placed on the top of the X-ray detector as a control (**f**). **g**, Photograph (left) and corresponding X-ray images (right) of an encapsulated metallic spring, recorded with a digital camera at time intervals from 1 s to 15 days. The Xr-LEI was performed by heating the flexible detector at 80 °C after cessation of X-rays (50 kV).



**Extended Data Fig. 10 | X-ray imaging of an electronic circuit board using a PDMS thin film containing  $\text{NaLuF}_4\text{:Tb(15 mol\%)}@ \text{NaYF}_4$  nanoparticles.** The X-ray exposure was controlled from 1 to 15 s, and the nanoparticle concentration in the PDMS film was controlled between 0.4 and 2.5 wt%.





**Extended Data Fig. 11 | Characterization of the stretchable X-ray detector.**

**a**, Material parameters were obtained by fitting the stress-strain curve of the elastomer using the Mooney-Rivlin model. Experimental results and analysis derived a tensile elastic modulus ( $E_t$ ) of 10 psi (0.0689 MPa), a tensile strength ( $\sigma_t$ ) of 200 psi (1.379 MPa), a Poisson ratio ( $\mu$ ) of 0.35 and a bulk modulus ( $D$ ) of 0.0766 MPa ( $C_{10} = 0.065$  MPa,  $C_{01} = 0.36$  MPa). **b**, Stress-strain curve of the film

in 10 cyclic stress-strain tests, with a sample width of 10 mm, a thickness of 1 mm, a gauge length of 50 mm and a loading rate of 100 mm min<sup>-1</sup>. **c**, Finite element simulation of strain distribution over the stretchable X-ray detector as the local strain increases to 500%. **d**, Light intensity function of pixels (along the blue line below and the full-width at half-maximum taken as the resolution) and X-ray imaging of a line-pair mask.